Axion-like Dark Matter Detection with Mercury-199 Atoms

Yi Chen

A dissertation
submitted in partial fulfillment of the
requirements for the degree of

Doctor of Philosophy

University of Washington

2018

Reading Committee:

Blayne R. Heckel, Chair

Subhadeep Gupta

Ann E. Nelson

Program Authorized to Offer Degree:
Department of Physics

University of Washington

Abstract

Axion-like Dark Matter Detection with Mercury-199 Atoms

Yi Chen

Chair of the Supervisory Committee:
Professor Blayne R. Heckel
Department of Physics

The objective of this dissertation is to search for axion dark matter through the coupling between the axion field and the electric dipole moment(EDM) of mercury-199 atoms. If the axion is the significant fraction of dark matter, the coupling leads to a time-varying nuclear EDM that oscillates at the frequency proportional to the axion mass, m_a. We use the data that measures the static EDM of ^{199}Hg atoms to look for a simple sinusoidal signal on the top of the static EDM value. The Lomb-Scargle periodogram, as a power spectrum estimator, allows us to analyze our unequally spaced EDM data in time. With two different approaches both with and without error weighting, they give a consistent result on no detection of dark matter. The most significant peak among the four EDM periodograms has a false alarm probability of 31% calculated with the Bootstrap method. The magnitude of the maximum peak can be generated by injecting a sinusoidal signal with the amplitude of 1.81×10^{-29} $e \cdot cm$. The smallest periodic signal our measurement can detect as the maximum peak in the periodogram with 95% confidence in the frequency range of 0 to 6.17×10^{-4} Hz is 2.3×10^{-29} $e \cdot cm$.

The static EDM of ^{199}Hg by itself is an important topic. This thesis will only briefly mention it and mainly cover the parts that are relevant to time-varying EDM analysis.

TABLE OF CONTENTS

LIST OF FIGURES

GLOSSARY

EDM: electric dipole moment

CMB: cosmic microwave background

DM: dark matter

CDM: cold dark matter

CP: charge parity

CPT: charge parity time

QCD: quantum chromodynamics

L-S PERIODOGRAM: Lomb-Scargle periodogram

FT: Fourier transform

FAP: false alarm probability

WIMPS: weakly interacting massive particles

ALPS: axion-like particles

ADMX: axion dark matter experiment

HV: high voltage

MT: middle top

MB: middle bottom

OT: outer top

OB: outer bottom

UW: University of Washington, Seattle, WA

ACKNOWLEDGMENTS

I would like to thank my adviser, Professor Blayne Heckel, for his essential guidance in my graduate studies. His enthusiasm on the precision experiment and his keen insight on the small but critical elements of the experiment have a great impact on my growth in research. Thank you, Blayne, for being available to me anytime to provide invaluable directions and feedback, for giving the freedom to explore the ways of analyzing data, and for your patience when the explorations got stuck.

This work would not be possible without the Professional Glassblower, Eric Lindahl, and the colleague, Brent Graner. I thank Professional Glassblower Eric Lindahl for providing not only his strong knowledge on the electronics, chemistry and physics but also his detailed and careful work to the experiment, especially constructing the Hg vapor cells from scratch with the remarkable lifetime which is critical in the experiment's precision. Brent is an experienced and outstanding experimentalist working with me closely. I thank Brent for his assistance on the laser system, the invaluable discussion about the details of the experiment, and the feedback on my talk.

In addition, I would like to thank many professionals and assistants: my mentors, Jacob Vanderplas and Professor Miguel Morales, who provided invaluable assistance and discussion on the periodic signal analysis; Professor Ann Nelson, who provided discussions on the theories of the dark matter; Professor Subhadeep Gupta, who encouraged me and gave me feedback on my thesis; Kyle Matsuda, for his assistance on the mapping of the magnetic field gradients that constrained the dominant systematic error; Alessandro Lindahl, who introduced me to the Python language and provided the assistance on various analysis methods.

I would not be able to reach this point without the support from my family, Hern-Chung Chen, Yu-Nan Lee and Jen-Chao Chen, and friends. A special thanks to Hsing-Wen Wang, Robin Brooks and Betty Lu for the pep talks and encouragement.

This research is supported by NSF Grant No. 1306743, No. 1707573 and the U.S. Department of Energy Office of Science, Office of Nuclear Physics under Award No. DE-FG02-97ER41020.

DEDICATION

to my dear parents, Hern-Chung Chen and Yu-Nan Lee

Chapter 1

DARK MATTER

The existence of dark matter(DM) in galaxies was concluded with detailed cosmological observations on the orbital velocities of interstellar matter in 1970[35]. By studying the cosmic microwave background(CMB), it has been shown that the baryonic matter only comprises a small fraction(less then 5%) of the total energy density in the Universe and the dark matter contributes about 27% of it[1][9]; however, DM has not been directly observed. Because DM does not seem to interact with electromagnetic radiation, such as light, and more specifically, it seems to only interact with gravity, DM cannot be any particle in the standard model and it is a challenge to determine what DM is made of. As we know so far, the dominant fraction of DM has the properties of being non-relativistic, non-baryonic, and stable[5]. The two most motivated candidates for DM are weakly interacting massive particles(WIMPs) and axion/axion-like particles(ALPs) because they not only have the properties of DM mentioned above but also can solve other long standing problems in particle physics[5].

The nuclear electric dipole moment(EDM) is a good probe to search for low energy dark matter[22] due to the coupling between dark matter field and gluons and quarks. The low energy dark matter can be thought of as a classical scalar field in space and causes the nuclear EDM to oscillate with its field. This thesis is to search for this time-varying EDM in the static EDM measurement.

1.1 WIMPs

WIMPs, standing for weakly interacting massive particles, are not a specific element but a broad class of possible particles[5]. They are expected to have the masses between 10

and 1000 GeV. The most motivated candidate for DM in WIMPs is the neutralino. It is a hypothetical particle in supersymmetric theories which may solve the gauge hierarchy problem. It is also used to calculate how many of them would still be around today assuming it is the dominant DM, and the number they end up with matches closely to the amount of dark matter experimentally observed. It is called WIMP miracle.

The WIMP experiments can be categorized as three varieties. The first is to detect them directly with the underground detectors while they are elastically scattered off nuclei, such as LUX[3] and XENON[4]. The second kind is to detect them indirectly by looking for radiation signals reaching Earth from space following collision and annihilation processes. These kinds of experiment usually have their detector pointing to the sky where there might be rich resources of DM, such as the Milky Way[10]. The third is to detect DM with powerful particle collisions, such as at the Large Hadron Collider at CERN[34].

1.2 Axion/Axion like particles

An axion is a hypothetical elementary particle first introduced by Peccei and Quinn in 1977 to be the solution of the strong CP (CP standing for charge parity) problem[31]. It is also recognized to be a well-motivated cold dark matter(CDM) candidate if its mass is within the range of 1-100 μeV[14]. Because its mass and all couplings are extremely small, it is also called the invisible axion. As a pseudo-Goldstone boson of a global symmetry that is broken at some scale, f_a, the axion decay constant, its couplings with radiation and matter are in the derivative form shown below:

$$\frac{1}{f_a}\mathrm{F}_{\mu\nu}\tilde{\mathrm{F}}^{\mu\nu}, \quad \frac{1}{f_a}\mathrm{G}_{\mu\nu}\tilde{\mathrm{G}}^{\mu\nu} \tag{1.1}$$

where F and G are the field tensors of electromagnetism and quantum chromodynamics(QCD). Its pure Goldstone nature could be broken leading to the generation of a mass, m_a, close to $\frac{\Lambda^2_{QCD}}{f_a}$, where Λ_{QCD} is the scale that QCD becomes strong. The axion decay constant, f_a, is expected to be $\mathcal{O}(10^{12} - 10^{17})$ GeV based on astrophysical bounds and cosmological bounds[14].

ADMX, standing for the axion dark matter experiment, is the most compelling axion experiment[14]. It uses a microwave cavity in a strong magnetic field to look for axion-photon coupling as shown on the left of Eq.1.1. In a static magnetic field, axions will decay into photons via the Primakoff effect. The energy of the photons is equal to the rest mass of the axion with a small contribution from its kinetic energy. The experiment is designed to detect axions with μeV mass range. Recently it has achieved the necessary sensitivity to detect the dark matter axion if they are at that mass range.

Like the QCD axion, axion-like particles(ALPs) are also good dark matter candidates[22]. Similar to the QCD axion, they are also pseudo-Goldstone bosons with ultralight mass and weak couplings to radiation and matter. They have less strict limitations and different sources of mass generation mechanisms than the QCD axion. Their mass depends not only on f_a but also on an additional parameter that depends on the mass generation mechanism.

1.3 Strong CP problem

The strong CP problem in particle physics is an unsolved physics question of why quantum chromodynamics(QCD) does not seem to break CP symmetry. The problem is the term in QCD Lagrangian that could violate the symmetry of CP:

$$L \supset \frac{g_s^2}{32\pi^2}\theta_{QCD} trG\tilde{G} \tag{1.2}$$

where G is the gluon field strength of QCD and g_s is the QCD gauge coupling. θ_{QCD} being non zero can create an electric dipole moment(EDM) of the neutron which would be comparable to $10^{-16}\theta_{QCD}\, e \cdot cm$ with θ_{QCD} unknown according to the Standard Model(SM) while the current experimental upper bound is $3.6 \times 10^{-26}\ e \cdot cm$ set by neutron EDM experiments[32] and the mercury EDM experiment[23].

$$d_n = 1.2 \times 10^{-16}\theta_{QCD} e \cdot cm \tag{1.3}$$

In the SM, there is no reason why θ_{QCD} is so small. For a long time, no theories could explain it. Until 1977, Peccei and Quinn proposed a compelling solution to the strong CP

problem by introducing an additional global $U(I)_{PQ}$ symmetry of the Lagrangian which has a mixed anomaly with QCD and a dynamical field, the axion[31][30]. The axion arises as the pseudo-Goldstone boson of the global $U(I)_{PQ}$ symmetry that is broken at a high scale f_a and the θ_{QCD} is dynamically tuned to zero while the axion redshifts towards the minimum of its potential. Therefore, solving the strong CP problem gives motivation to discover new physics beyond the SM.

1.4 Matter-Antimatter Asymmetry

The SM of elementary particles, containing the knowledge of electromagnetic, weak, and strong interactions, has successfully provided experimental predictions in many cases but falls short to explain the experimental observation of the asymmetry between matter and antimatter. In 1967, a remarkable paper from Sakharov established that three conditions were required in the early Universe to cause the matter-antimatter asymmetry now[36]:

•Baryon number violation

•Violation of charge conjugation(C) symmetry and the combined charge conjugation parity(CP) symmetry, and

•Departure from thermal equilibrium

Both CP violation sources in the SM, θ_{QCD} in the strong forces and the phase, n, in the CKM matrix in weak interactions, are still not enough to explain the baryon asymmetry. Therefore, extensions to the SM are necessary to resolve it. The Supersymmetry models, the grand unified theories, and the models with right handed neutrinos, which are well-known extensions, all include much more P and CP violation sources. Low energy experiments, such as the measurements of electric dipole moments, provide essential constraints to such extension theories of the SM. The Hg EDM experiment especially provides great information on both CP violation beyond the SM and θ_{QCD} CP violation.

1.5 Oscillating nuclear EDM

In an addition to the θ_{QCD} axion with an energy range from 0.5 μeV to 1 meV, there might be some other kinds of axions outside of this range that are also dark matter. Peter Graham from Stanford University proposes that ultralight particles such as the axion and ALPs can be thought of as a background classical field coupling with gluons and quarks and then lead to a time-varying nuclear EDM[21][22]. It is under the assumption that these ultralight particles have a large number density and are a significant fraction of the dark matter. Consequently, the oscillation can be described in the form: $a = a_0 \cos(\frac{m_a c^2}{\hbar} t)$ with amplitude a_0 set by the energy density and the frequency proportional to the dark matter mass, m_a. Depending on the mass generation mechanism, the mass of the dark matter can be generated from different sources. For example, θ_{QCD} axion first introduced by Peccei and Quinn has a mass proportional to $\frac{1}{f_a}$ where f_a is the axion decay constant.

Unlike other current experiments searching for the axion or ALPs through their coupling with the photon and limited by the coverage of the mass above meV, this time-varying EDM is a new detector for dark matter with mass $m_a \lesssim 10^{-9}$ eV, corresponding to a theoretically well-motivated axion decay constant, $f_a \gtrsim 10^{16} GeV$.

Chapter 2
INTRODUCTION TO EDM

An electric dipole moment is defined by a pair of opposite charges($\pm q$) separated by a distance x, giving an EDM of $\mathbf{d} = q\mathbf{x}$, where $\mathbf{x}$ is pointing from $-q$ to $+q$. For a distribution of charges with charge density $\rho(\mathbf{r})$, the edm is defined as:

$$\mathbf{d} = \int \rho(\mathbf{r})\, \mathbf{r}\, \mathrm{d}^3 r \tag{2.1}$$

2.1 Atomic EDMs

A permanent EDM of an atom can be thought of as the result of how the electrons and nuclei distribute in an atom. An atomic EDM arises from the mixing of opposite parity wave functions generated by intrinsic EDMs of the constituents and a P,T-odd interaction $\hat{H}_{PT}$ [20].

The atomic EDM induced in an atomic state, K, due to admixture with the opposite-parity wave functions M is given by

$$\mathbf{d}_{atom} = 2\sum_{M} \frac{\langle K|\hat{\mathbf{D}}|M\rangle\langle M|\hat{H}_{PT}|K\rangle}{E_K - E_M} = d_{atom}(\frac{\mathbf{F}}{F}) \tag{2.2}$$

where $\hat{\mathbf{D}} = -e\sum_i \mathbf{r}_i$ is the electric dipole operator, $\hat{H}_{PT}$ is the P,T-odd operator that mixes K with the set of wave functions M, and F is the total angular momentum of the atom corresponding to the state K. An atomic EDM is directed along the total angular momentum F, the only vector specifying the system.

2.2 Mechanisms that induce an atomic EDM

A typical EDM experiment is conducted under parallel electric and magnetic fields. The Hamiltonian for a spin $\frac{1}{2}$ system is:

$$\hat{\boldsymbol{H}} = -\boldsymbol{\mu} \cdot \mathbf{B} - \mathbf{d} \cdot \mathbf{E} \tag{2.3}$$

By reversing the direction of the electric field, the linear Stark shift can be easily obtained by measuring the change in frequency.

Without considering relativistic effects and the finite-size of nucleus, the charges inside a neutral atom under an external electric field will redistribute themselves perfectly to cancel the external electric field such that there is no atomic EDM induced. However, if magnetic, relativistic or finite-size effects are taken into account, the electron shielding is incomplete so an atomic EDM can be induced as shown by Schiff[39].

Four mechanisms that can induce an atomic EDM are: an electron EDM, a P,T-odd electron-nucleon interaction, a nucleon EDM, and a P,T-odd nucleon-nucleon interaction. Each atomic EDM typically is induced by multiple mechanisms with different sensitivity levels. For instance, ^{199}Hg EDM is most sensitive to P,T-odd nuclear forces, nucleon-nucleon and electron-nucleon interactions, but it also has sensitivity to the static EDM of the neutron and electron. The neutron EDM experiment is a special case that only measures the intrinsic neutron EDM.

Different EDM species and systems have various sensitivities to mechanisms inducing an atomic EDM. For instance, the paramagnetic systems, with nonzero total electron angular momentum, are most sensitive to electron EDM but the diamagnetic systems, with zero total electron angular momentum, are most sensitive to P,T-odd mechanisms in the hadronic sector. Therefore, it is important to search for EDMs in different systems to gather complementary information to understand the underlying physics.

2.3 the Schiff moment

The last two EDM mechanisms in the previous section, nucleon EDMs and P,T-odd nucleon-nucleon interactions, are often grouped together because they are both at the nuclear scale and produce P,T-odd nuclear multipole moments. In our mercury EDM experiment, it is most sensitive to the nuclear Schiff moment due to the nucleon distribution. This section is the detail of how to obtain the Schiff moment from the setup of a neutral atom under an external electric field.

An external electric field acting on a neutral atom, before considering the finite size of the nucleus and relativistic electrons near the nucleus, is screened at each particle. Because the neutral atom is not accelerating, the net electric force exerting on the atom is zero without considering magnetic forces. The electrostatic potential of the nucleus can be shown below[20][41]:

$$\varphi(\mathbf{R}) = \int \frac{e\rho(\mathbf{r})}{|\mathbf{R}-\mathbf{r}|}\mathrm{d}^3r + \frac{1}{Z}(\mathbf{d}\cdot\nabla)\int \frac{\rho(\mathbf{r})}{|\mathbf{R}-\mathbf{r}|}\mathrm{d}^3r \tag{2.4}$$

where $\nabla_i \equiv \frac{\partial}{\partial R_i}$, $\rho(\mathbf{r})$is the nuclear charge density, $\int\rho(\mathbf{r})\mathrm{d}^3r = Z$, and

$$\mathbf{d} = \int e\mathbf{r}\rho(\mathbf{r})\mathrm{d}^3 = d\frac{\mathbf{I}}{I} \tag{2.5}$$

is the P,T-odd nuclear EDM. Naively the second term in Eq.2.4 is expected to be the first leading P,T-odd term in this electrostatic potential; However, the first expansion term is actually canceled by the second expansion term of the first term of Eq.2.4 after Taylor expansion. Therefore, there is no first-order interaction between the dipole and the field[39]. And the first nonzero P,T-odd term in Eq.2.4 can be repackaged to $\varphi_{octupole} + \varphi_{Schiff}$ where

$$\varphi_{octupole} = -\frac{1}{6}O_{ijk}\nabla_i\nabla_j\nabla_k\frac{1}{R} + \frac{1}{e}\frac{1}{2Z}Q_{ij}(\mathbf{d}\cdot\nabla)\nabla_i\nabla_j\frac{1}{R} \tag{2.6}$$

$$\varphi_{Schiff} = 4\pi\mathbf{S}\cdot\nabla\delta^3(\mathbf{R}) \tag{2.7}$$

S is the P,T-odd nuclear Schiff moment, O_{ijk} is the P,T-odd nuclear electric octupole moment, and Q_{ij} is the P,T-even nuclear electric quadrupole moment. The nuclear Schiff moment is given by

$$\mathbf{S} = \frac{1}{10}\Big[\int e\rho(\mathbf{r})\mathbf{r}r^2\mathrm{d}^3r - \frac{5}{3}\mathbf{d}\frac{1}{Z}\int \rho(\mathbf{r})r^2\mathrm{d}^3r\Big] = S\mathbf{I}/I \tag{2.8}$$

P,T-odd nuclear moments, such as Schiff moments, induced by the nucleon-nucleon interactions are typically 10-100 times larger than the ones arising by a nucleon EDM[20]. And it is why the mercury EDM generated by the Schiff moment can set a tighter constraint on many CP-violating parameters than the result of neutron EDM does.

2.4 Nuclear enhancement mechanisms

The atomic nucleus consists of nucleons, protons and neutrons. The number of nucleons strongly affect the shape and the properties of the nucleus. If the nuclei have a certain number of protons and a certain number of neutrons(called the magic number), they are very stable and have spherical shape. However, the ones with extra nucleons beyond the magic numbers, the long-range effective forces between the valence nucleons distort the shape from spherical symmetry and the nuclei are deformed[2].

The nuclei without spherical symmetry can have an enhanced sensitivity to CP violation due to the small energy separation between states of opposite parity and the same angular momentum as the ground state[16]; see Eq.2.2. Radium is a good example of nuclear octupole deformation. Due to the collective interactions between nucleons, the nucleus deforms to a pear shape with energy eigenstates being opposite parity states of the symmetric and anti-symmetric sum of the pear and inverted pear. The radium Schiff moment is expected to be several hundred times larger than ^{199}Hg whose nucleus has spherical symmetry[20].

Chapter 3

EDM EXPERIMENT

The measurement of the permanent electric dipole moment of mercury 199 has been improving almost linearly in a log graph with time shown in the figure below since the first published result in 1987. This chapter addresses the reasons why mercury 199 is a good candidate to search for an electric dipole moment, the advantage of this experiment over other EDM groups and the most recent result on Hg EDM.

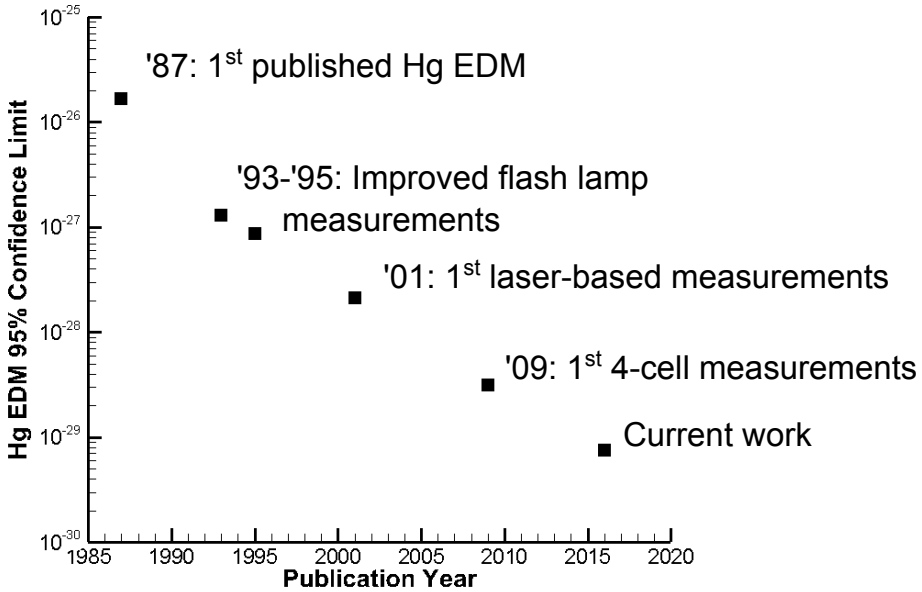

Figure 3.1: Improvement of the Hg EDM measurement

3.1 Heavy atom with an unpaired neutron

Hg is a good element to search for a nuclear EDM because it is a heavy atom with nuclear charge Z equal to 80. As mentioned in section 2.3, the Hg EDM is most sensitive to the Schiff moment arising from the nucleon-nucleon interaction.

From Eq.2.6 to Eq.2.8, it shows that the P,T-odd part of the electrostatic nuclear potential is mainly from inside of the nucleus. An atomic EDM induced by the interaction of electrons with Schiff moment is proportional to the Schiff moment and the amplitude of the electronic wave function at the nucleus. The interaction $\hat{H}_{PT}$ in Eq.2.2 can be shown as $-e\sum_i \varphi^i_{Schiff}$ and it mixes the opposite parity electron orbitals, s and p.

$$\langle s| - e\varphi_{Schiff}|p\rangle = 4\pi e\mathbf{S}\cdot(\nabla\psi_s^\dagger\psi_p)_{R=0} \tag{3.1}$$

The Schiff moment is a r^3-weighted integral over the difference in the nuclear charge and EDM distributions shown in Eq.2.8 so it increases with the nuclear charge Z. The second part, $\psi_s^\dagger\psi_p$ inside the nucleus, is proportional to $Z^2\alpha^2$ where α is the fine-structure constant and Z is the nuclear charge. And that is why heavy atoms are favored in the studies of T,P-odd moment.

The Hg EDM not only is sensitive to the Schiff moment but also gives competitive limits on the neutron EDM and proton EDM. The nucleus of ^{199}Hg has an unpaired valence neutron. The limit on the neutron EDM extracted from ^{199}Hg is competitive with the best bare neutron EDM experiment at Paul Scherrer Institute(PSI). Not only so, it also sets a tighter constraint on the proton EDM than the TlF molecule used to set the proton EDM upper limit.

3.2 the Advantages of Hg experiment over others

The three leading ongoing nuclear EDM experiments are the bare neutron EDM at PSI, the Hg EDM at University of Washington and the Ra EDM at Argonne National Laboratory. They have different sensitivities to various mechanisms that induce an EDM. The funda-

mental limit on the sensitivity for these experiments can be estimated by using the formula for the energy splitting:

$$\delta d = \frac{\hbar \delta \omega}{2E} \tag{3.2}$$

where ω goes as $\frac{1}{\tau}$ for a single particle with spin coherence time τ. With a number N of samples, the uncertainty is reduced by $\sqrt{N}$. A number of $\frac{T}{\tau}$ independent measurements can be performed, reducing the uncertainty by $\sqrt{\frac{T}{\tau}}$ with the total integration time T. Therefore, the lower bound of the uncertainty is:

$$\delta d = \frac{\hbar}{2E\sqrt{N\tau T}} \tag{3.3}$$

The following subsections will discuss the advantage of the Hg EDM experiment over other experiments based on its sensitivities according to Eq. 3.3.

3.2.1 Multiple measurements simultaneously

The biggest advantage of the Hg EDM experiment over other EDM groups is that we can store $\sim 10^{14}$ Hg atoms in small vapor cells and perform an unlimited number of spin precession measurements. We also have the ability to measure the mercury atoms precession frequencies under different field configurations at the same time. Therefore, we can remove the common mode noise from the signal and extract the EDM signal directly. A few reasons that enable us to do it are: first of all, it is a table-top experiment with a comparatively simple data taking routine because it involves neither complicated procedures, like transferring samples to a detected region, nor big-scale operation, such as a nuclear reactor. Secondly, the large room temperature vapor pressure of Hg allows us to store the atoms in a fused silica vapor cell shown in figure 3.2 and operate it at room temperature. As a result, a large number of samples N and an extra factor of $\frac{1}{\sqrt{2}}$ from the apparatus setup can increase the sensitivity of each measurement; see Eq.3.3.

The mercury vapor cell which holds mercury in place in the apparatus has a cylindrical shape and is prepared in a vacuum system to avoid any contamination. Making a mercury

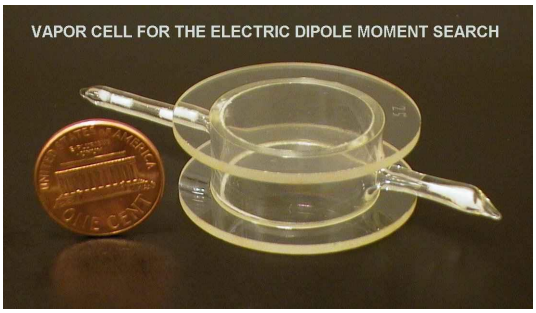

Figure 3.2: EDM vapor cells with 25-mm inner diameter and 10.1-mm height. They are fabricated from Heraeus Suprasil fused silica and filled with 0.56 atm of CO buffer gas and 0.5 mg of isotopically-enriched ^{199}Hg

cell with a long coherence lifetime is an art even though there are only few elements inside: mercury isotope 199, CO and wax. The detailed procedure of fabricating a Hg vapor cell is addressed in [24]. Once the mercury vapor cell is built and prepared, it does not require much additional work during data taking. In comparison with other EDM experiments, such as Ra and the neutron EDM experiments, the signal source cannot be stored in a vapor cell so it needs to be confined or even transferred to a specific detected region by optics techniques. For example, Ra atom's vapor pressure is too low to operate in a vapor cell so laser cooling and trapping are required to measure Ra's EDM[8]. Ultra-cold neutrons from a nuclear reactor are confined by a material medium providing a step potential relative to vacuum for long-wavelength neutrons[6]. During the process it is really common to lose a big portion of the samples. Therefore, one of their challenges is to maintain as many samples as they can throughout the process.

The mercury experiment gains sensitivity through the large number of atoms in a vapor cell. The mercury vapor cell with 25 mm inner diameter and 10.1 mm in height is filled

with 0.56 atm of CO buffer gas and ~ 0.5 mg of isotopically-enriched mercury 199 and wax. The ideal gas law says that about 10^{14} atoms are in the vapor phase in a vapor cell. For Ra[8] and neutron EDM experiment[32], they can only obtain about 10^3 to 10^5 particles after transferring samples to the detected region.

The ability of measuring multiple field configurations simultaneously not only allows us to remove the common mode magnetic field noise but also increase the sensitivity of each measurement by $\sqrt{2}$. The Mercury EDM measurement consists of a stack of total of four cylindrical mercury vapor cells sitting inside of a grounded conducting plastic vessel under a common magnetic field shown in Fig.3.3. The outer two cells are placed inside the high voltage(HV) electrodes connecting to HV so they don't see potential difference across them and serve as magnetometers. The middle cells have a ground plane sandwiched between them and another side of the middle cells is in contact with the HV electrodes. Therefore, the middle two cells experience an opposite direction of the electric field relative to the magnetic field's direction. By comparing the frequency difference between the middle two cells, twice the energy shift due to the EDM interaction with the electric field can be obtained which increases the sensitivity of the measurement by 2 and also adds additional noise by $\sqrt{2}$ with the assumption that all the individual measurement are independent.

3.2.2 Long lifetime and interrogation time

The sensitivity of the measurement increases as the square root of coherence time and the total integration time shown in Eq.3.3. Therefore, the long coherence time of the mercury vapor cell is essential in this experiment. And it is also one of the biggest breakthroughs in the most recent Mercury EDM result[23]. Fabricating a vapor cell with long coherence time is very challenging because it involves lots of unknown chemical interactions among different elements in the cell. In the most recent result on the mercury EDM, the four cells have coherence time from 250 seconds to 600 seconds. Comparing with 100 seconds in 2000's result and 200 seconds in 2009's result, this breakthrough allows us to apply the Ramsey's method to detect the EDM signal. Instead of watching the mercury atoms precess about the

magnetic field for a long period of time under the probing laser as the previous Hg EDM experiments did, the Hg atoms are set to precess in the dark without any interaction with the laser for 170 seconds between two 30-second short laser probings. These two short probes allows us to read the initial and final phases right before and after the laser turns off and on to determine the actual precession frequency in the dark. The precession in the dark not only avoids the laser decreasing the coherence time but also eliminates any systematic effect due to the interactions with the laser. Comparing with our 170-second coherence time in the dark in one cycle of our Hg EDM measurement, Ra atoms precess under the probing laser for 40 seconds and neutrons for 130 seconds.

3.3 The result of mercury 199

Our results[23] for this frequency shift are consistent with zero; we find the corresponding ^{199}Hg EDM $|d_{Hg}| = (2.20 \pm 2.75_{stat} \pm 1.48_{syst}) \times 10^{-30} e \cdot cm$. We use this result to place a new upper limit on the ^{199}Hg EDM $|d_{Hg}| < 7.4 \times 10^{-30} e \cdot cm$ (95% C.L.), improving our previous limit by a factor of 4. More details about the static EDM are addressed here[24].

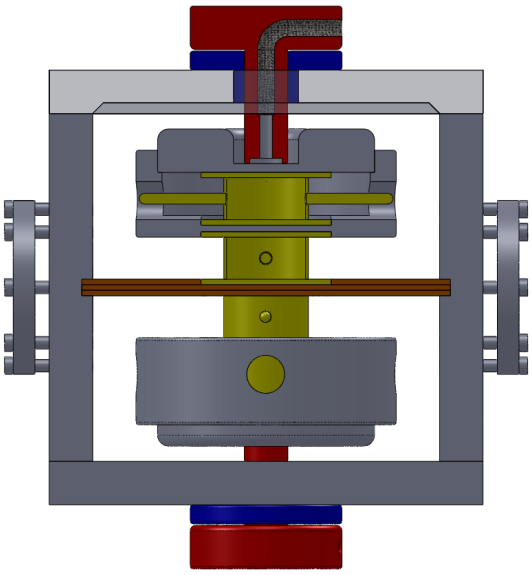

Figure 3.3: An simplified illustration on the EDM apparatus. The EDM vessel(dark gray) and the two HV electrodes(dark gray) are made out of the same material, graphite-filled polyethylene, to make them conductive. The front and back walls of the vessel are removed to show the details inside. Inside the EDM vessel, the top half is the cross sectional view of the HV feedthrough(red), the HV feedthrough guide(blue), the top HV electode(dark gray), the outer top vapor cell(yellow), the middle top vapor cell(yellow), and the ground plates(brown). The vapor cell has two stems on two sides perpendicular to the light beam's propagation. The two circles in the middle of the two middle vapor cells are the stems pointing out of page.

Chapter 4

STATIC EDM

The existence of the static EDM causes a small energy shift shown in the Larmor precession frequency due to the interaction with an external electric field. This chapter describes the analysis methods this experiment uses to extract the EDM signal and look for systematic effects.

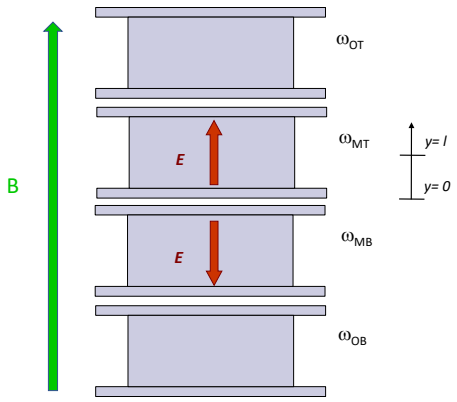

Figure 4.1: A simplified drawing of the stack of four cells under a common magnetic field. Only the middle two cells experience the electric field across them.

4.1 Four cell magnetometry

The Hg experiment consists of four Hg cells in a stack in a vertical arrangement such that it gives us many frequency combinations to extract the EDM signal and to observe potential systematic effects. The four cells are symmetrically placed relative to the median plane of

the apparatus under a common vertical uniform magnetic field. The magnetic field can be expanded at the center of apparatus with $y = 0$ and the cells locate at $y = \{-3l, -l, l, 3l\}$.

$$B(y) = B(0) + B'(0)y + \frac{1}{2}B''(0)y^2 + \frac{1}{6}B'''(0)y^3 + O(y^4) \tag{4.1}$$

where $' = \frac{d}{dy}$.

According to Eq.2.3, the energy shift for an atom with an EDM under parallel magnetic and electric fields is $\hbar\omega$ equal to $-\mu \cdot B - d \cdot E$. In one of the four Hg EDM field configurations, the four cells are under a common uniform upright magnetic field but only the two middle cells experience an electric potential difference across them and pointing outwards from the median plane shown in Fig 4.1. The outer two cells are inside of conducting plastic high voltage electrodes so they do not see an electric field across them. Plugging the cells' distances corresponding to the medium plane in Eq.4.1, Larmor frequencies for these four cells are:

$$\omega_{OT} = -\frac{\mu}{\hbar}\Big[B(0) + 3lB'(0) + \frac{9}{2}l^2B''(0) + \frac{9}{2}l^3B'''(0)\Big] \tag{4.2}$$

$$\omega_{MT} = -\frac{\mu}{\hbar}\Big[B(0) + lB'(0) + \frac{1}{2}l^2B''(0) + \frac{1}{6}l^3B'''(0)\Big] - \frac{d}{\hbar}E \tag{4.3}$$

$$\omega_{MB} = -\frac{\mu}{\hbar}\Big[B(0) - lB'(0) + \frac{1}{2}l^2B''(0) - \frac{1}{6}l^3B'''(0)\Big] + \frac{d}{\hbar}E \tag{4.4}$$

$$\omega_{OB} = -\frac{\mu}{\hbar}\Big[B(0) - 3lB'(0) + \frac{9}{2}l^2B''(0) - \frac{9}{2}l^3B'''(0)\Big] \tag{4.5}$$

where the subscript of OT, MT, MB, and OB are the short scripts for the outer top cell, middle top cell, middle bottom cell and outer bottom cell. From here, it is clear to see the frequency combinations from different cells shown in table 4.1.

The frequency combinations in table 4.1 can be categorized as two-cell, three-cell and four-cell combinations. In the actual measurement, the Larmor precession frequency is the average frequency of all the atoms in the volume of the vapor cell but here the cells are treated as point objects for the analysis purpose. The zero-order field fluctuation is not listed in one of the columns because taking the frequency difference between cells removes the common-mode magnetic field.

Frequency combination	Magnetic + EDM contributuin			
	$\frac{\mu}{\hbar} lB'(0)$	$\frac{\mu}{\hbar} l^2 B''(0)$	$\frac{\mu}{\hbar} l^2 B'''(0)$	$\frac{d}{\hbar} E$
$\omega_{MT} - \omega_{MB}$	2		$\frac{1}{3}$	2
$\omega_{OT} - \omega_{OB}$	6		9	
$\omega_{OT} - \omega_{MT}$	2	4	$\frac{13}{3}$	-1
$\omega_{MB} - \omega_{OB}$	2	-4	$\frac{13}{3}$	-1
$\omega_{OT} - \omega_{MB}$	4	4	$\frac{14}{3}$	1
$\omega_{MT} - \omega_{OB}$	4	-4	$\frac{14}{3}$	1
$\omega_{MT} - \frac{1}{2}\omega_{MB} - \frac{1}{2}\omega_{OT}$		-2	-2	$\frac{3}{2}$
$\omega_{MB} - \frac{1}{2}\omega_{MT} - \frac{1}{2}\omega_{OB}$		-2	2	$-\frac{3}{2}$
$\omega_{MT} - \frac{2}{3}\omega_{OT} - \frac{1}{3}\omega_{OB}$		-4	$-\frac{4}{3}$	1
$\omega_{MB} - \frac{2}{3}\omega_{OB} - \frac{1}{3}\omega_{OT}$		-4	$\frac{4}{3}$	-1
$\omega_{OT} + \omega_{OB} - (\omega_{MT} + \omega_{MB})$		8		
$\omega_{MT} - \omega_{MB} - \frac{1}{3}(\omega_{OT} - \omega_{OB})$			-$\frac{8}{3}$	2

Table 4.1: List of the linear combinations of cell precession frequencies that we regularly monitor in terms of the uniform field expanding at the center of the apparatus. The numbers shown on the right are the coefficients of the field gradient with different orders.

The first six channels are the two-cell frequency differences. $\omega_{MT} - \omega_{MB}$ is sensitive to EDM signal but also has contribution from linear field gradient. $\omega_{OT} - \omega_{OB}$ is most sensitive to the linear field gradient among all the monitored channels and the piece of linear field gradient is expected to be three times bigger than what $\omega_{MT} - \omega_{MB}$ has due to three times larger distance between the cells. Because it is insensitive to EDM signal, the average value should be zero and should be consistent with zero within the error bar. Therefore, it is used to look for potential systematic effects.

The next four frequency combinations in table 4.1 include three cells to remove field gradients up to the linear term so they are most sensitive to the second-order field gradient.

The top two have both MT's and MB's frequencies in the frequency combinations and are 1.5 times more sensitive to EDM signal than a single cell by itself. They can show a more meaningful result than the four-cell frequency combination($\omega_{MT} - \omega_{MB} - \frac{1}{3}(\omega_{OT} - \omega_{OB})$) if one and only one of the outer cells is acting out of whack. For the same reasons, another two three-cell frequency combination can be very useful if one and only one of the middle cell is not running normally.

$\omega_{MT} - \omega_{MB} - \frac{1}{3}(\omega_{OT} - \omega_{OB})$, the "EDM combo", gives us the most sensitive EDM signal among all and is immune to the field fluctuations up to the second order. $\omega_{OT} + \omega_{OB} - (\omega_{MT} + \omega_{MB})$ is another four-cell combo. It is also called a "leaktest" combo and has zero contribution from a true EDM. Therefore, it is used for systematic error tests, especially the systematic acting like second-order field fluctuations. We concentrate upon the EDM combo, leaktest and $\omega_{OT} - \omega_{OB}$.

4.2 HV sequence, string analysis, and data taking routine

The middle two cells shown in Fig.4.1 are EDM sensitive because only these two cells have an electric fields across them. During EDM data taking, the HV sequence switches the electric field direction between pointing outwards and pointing inwards such that the EDM combo channel is sensitive to $2\frac{d}{\hbar}E$ and some third order field gradient for one run and sensitive to $-2\frac{d}{\hbar}E$ and some third order field gradient for the next run. With only a nonzero EDM, the EDM measurement is expected to obtain a data jump between $2\frac{d}{\hbar}E$ and $-2\frac{d}{\hbar}E$. However, the signal is much smaller than the magnetic field drift. The left panel in Fig.4.2 shows an overnight run with 274 points. Each point is a 250-second scan. The shift in the frequency difference of EDM combo is about 400 $n\,rad/s$ over a night due to the change of the third order field gradient along the 4-cell axis. To remove this slow drift, we apply three-point string analysis such that:

$$\Delta\omega_i^{new} = (-1)^i \frac{\Delta\omega_{i-1} + \Delta\omega_{i+1} - 2\Delta\omega_i}{4} \tag{4.6}$$

Therefore, all the points in $\Delta\omega^{new}$ measure the same quantity $2\frac{d}{\hbar}E$ shown in the right

panel in Fig.4.2. Without the string analysis, the result is dominated by the slow drift in time. Because of this string analysis, the EDM data points, $\Delta\omega^{new}$, correlate with the two neighboring points ahead and another two neighboring points behind.

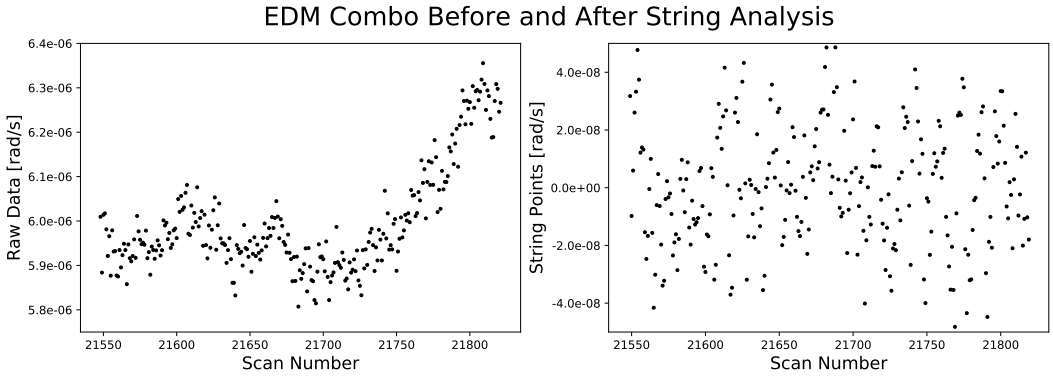

Figure 4.2: These two panels are a typical overnight run before and after string analysis. The left panel is the raw data of EDM combo. This run is consisted with 274 scans and the cycle time is 250 seconds. The overall drift is dominated by the field gradient shift in time. The right panel is the EDM values after applying string analysis on the raw data. All the string points in the right panel are correlated with two neighboring points ahead and behind it.

About the EDM data taking routine, one overnight run is usually about 12 to 15 hours and it is consisted with 220 to 250 scans. Each scan is about 270 to 285 seconds. Every morning, we stopped the run and took another short measurement with the HV sequence being 0, +, 0, - to look for systematic effects instead of the regular HV sequence setting, +, -, +, -, for the overnight runs. Then, we would fine tune the optics and adjust the apparatus to make sure all the setups are in the best shape. Like the change on the HV sequence, there are other parameters we changed on the regular basis for systematic effects analysis. It includes the change in HV value between 6kV and 10kV, two HV ramp rates, two magnetic field directions. There are total eight different configurations. One sequence is consisted with two sets of these eight configurations. It usually takes about one month to complete. After that, we rotated the positions of the four cells for a new sequence. About the halfway through the EDM measurement, we also modified the vessel which holds the four cells and HV

feedthroughs in place. All the pauses and stops, such as extra measurement for systematic effects study and apparatus maintenance, during the EDM measurement have shown as gaps in time in Fig.6.1. Searching for the time-varying EDM signal in such unevenly spaced data requires another algorithm other than Fourier transform spectrum to characterize the periodic signals in the unevenly-sampled data.

Chapter 5

OSCILLATING EDM

As described earlier, ultra light particles such as an axion or ALPs can couple with gluons and quarks and then lead to an oscillating nuclear EDM. The ^{199}Hg static EDM measurement[23] is used to look for the possible oscillation on the top of the static EDM value. The EDM data taking routine has an almost 24/7 schedule but it pauses everyday for a short time to reset and maintain the apparatus conditions. For such unevenly sampled data, the power spectrum calculated from Fourier transform(FT) fails to present the actual power density of the underlying continuous signal. Instead, the Lomb-Scargle(L-S) periodogram is used in the analysis to detect the simple sinusoid periodic signal. As the result, the size of the most significant peak in the EDM periodograms can be generated by an injected periodic signal with an amplitude of 2.3×10^{-29} e·cm and we conclude our EDM dataset can identify an oscillating signal with the magnitude of 1.81×10^{-29} e·cm as a largest peak with 95% confidence in the frequency range between 0 Hz and 6.17×10^{-4} Hz.

5.1 Introduction on classical periodogram and Lomb-Scargle periodogram

Periodogram is a technique commonly used especially in the field of astronomy to look for possible periodic signals in unequally spaced time series. It is similar to the Fourier power spectrum in the way that both of them are interested in extracting the frequency information in the signal. However, conceptually they are two different things.

The classical periodogram, also called the Schuster periodogram, was first proposed by Schuster in 1898. It has the exact form of the power density calculated from FT besides the normalization factor, $\frac{1}{N}$, where N is the number of data points(see Section 5.3.1). However, its statistical property is no longer retained when data is unequally spaced in time. In 1976,

based in part on earlier work by Barning and Vanicek, Lomb developed the periodogram with the least-squared method. It not only greatly mitigates the difficulties of the previous periodgrams but also includes additional features. The Lomb-Scargle periodogram, sometimes called standard periodogrm, is the result Scargle elaborated from Lomb's work in a systematic way. It is well-motivated and widely accepted due to its three properties. First of all, L-S periodogram reduces to the classical form in the case of equally spaced time series. Second, the periodogram's statistics is analytically computable. Third, the periodogram is insensitive to global time shift. Therefore, L-S periodogram is the first method to use when analyzing periodic signals, especially a simple sinusoid signal in an unevenly-spaced time series.

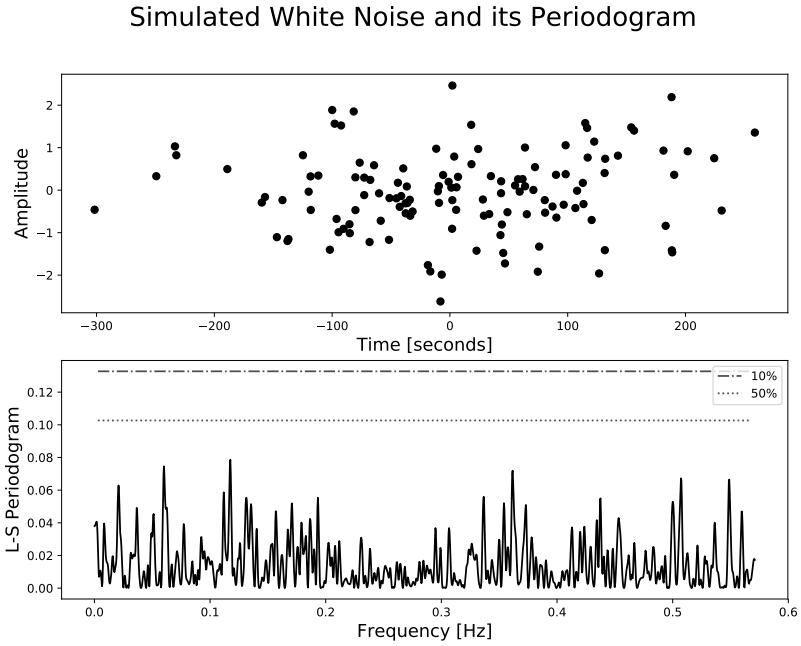

Figure 5.1: Example of the Lomb-Scarlge periodogram of pure Gaussian noise. The upper panel is the raw data of 128 points. They are Gaussian distributed at random times between 0 and 100 seconds with zero mean and .5 standard deviation. The bottom panel is its Lomb-Scargle periodogram with the significant levels of 10% and 50% calculated by the bootstrap method.

Figure 5.1 shows the results of applying Lomb-Scargle periodogram as discussed above. In the upper panel, the raw data is plotted against time. The 128 data points are randomly distributed in time and the value is Gaussian distributed with expected zero mean and the standard deviation of 0.5. The bottom panel is the periodogram of the raw data. The horizontal lines are significance levels, 0.5 and 0.1. The significance level is estimated with bootstrap method which is explained in section 5.4. As a note, significant level and false alarm probability(FAP) are used interchangeably. It is a method to measure how likely the peak is caused by noise. You may think of the significance level as being 1-CF, where CF is the tradition "confidence level".

Figure 5.2 shows the raw data with an injected fake signal with amplitude of .5 and frequency of .398 Hz. The upper panel is the amplitude of the signal against the time and the bottom figure is the Lomb-Scargle periodogram with a peak corresponding to the injected signal with significance level of 10^{-1}.

5.2 What does the FT output: Evolution theorem

Any signal can be decomposed to sine and cosine waves with various amplitudes and frequencies. The Fourier transform is a method that decomposes the signal, a continuous function of time, into frequencies that comprise. The squared amplitude of the FT at each frequency grid presents the power component at that frequency in the underlying continuous signal. This Fourier-driven power spectrum is commonly used to analyze periodic signal for data evenly spaced in time. However, it fails to present the correct amount of power in the frequency base when data are not sampled with a fixed sampling rate. By looking into the property of the FT: evolution theorem, it gives a clear explanation on what the FT does on the data and what we actually obtain from the FT.

The FT of a signal, g, is denoted by adding a circumflex: $\hat{g}$. For a continuous time series g(t) infinite in length, its FT is symbolically presented as $\hat{g}(f)$ or $\mathcal{F}\{g(t)\}$ in Eq.5.1 and calculated by the formula in Eq.5.2.

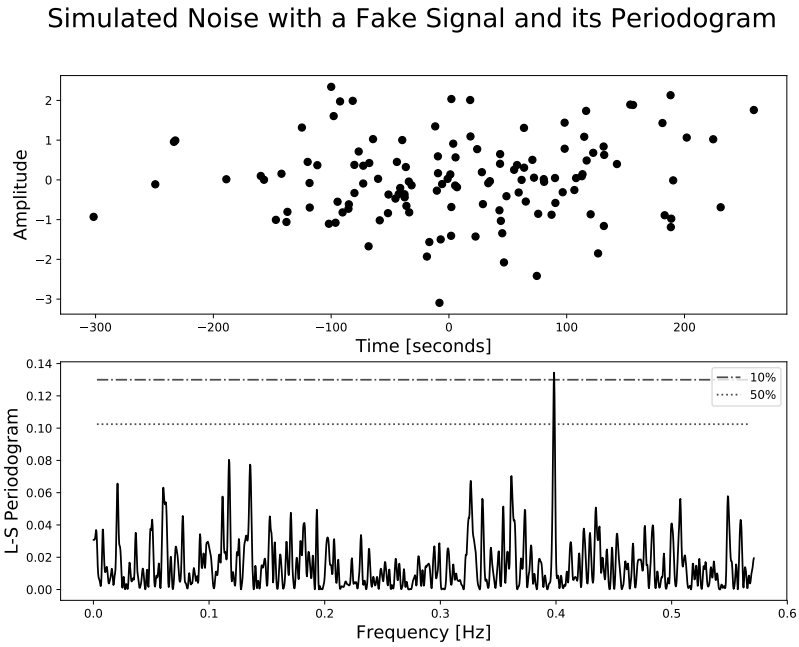

Figure 5.2: Example of Lomb-Scargle periodogram with Gaussian noise and an injected signal. In the upper panel, the fake signal with an amplitude of .5 and frequency .398 Hz is injected to the raw data, 128 Gaussian distributed data points at random times between 0 and 100 seconds with zero mean and .5 standard deviation. The bottom panel shows its Lomb-Scargle periodogram has a peak corresponding to the injected signal with the significance level of 10%.

$$g(t) \underset{\text{FT}}{\longrightarrow} \hat{g}(f), \mathcal{F}\{g(t)\} \tag{5.1}$$

$$\hat{g}(f) = \int_{-\infty}^{\infty} g(t) \mathrm{e}^{-2\pi i f t} dt \tag{5.2}$$

The convolution theorem shows the Fourier transform of a convolution of two functions, $\mathcal{F}\{g * f\}$, is equivalent to the point-wise product of the individual Fourier transforms shown in Eq.5.3.

$$\mathcal{F}\{g * f\} = \mathcal{F}\{g\} \cdot \mathcal{F}\{f\} \tag{5.3}$$

where * denotes convolution in this context, and not multiplication. And $\cdot$ denotes point-wise multiplication. It always works in another way:

$$\mathcal{F}\{g \cdot f\} = \mathcal{F}\{g\} * \mathcal{F}\{f\} \tag{5.4}$$

Fig.5.3 illustrates the second case of the evolution theorem in Eq.5.4 for the case with a fixed sampling rate. The three right panels are the Fourier transform of the function on their left. The top left panel is the underlying continuous signal we are trying to measure. Here the Gaussian signal is chosen as the example. In reality, even though we can sample the signal so fast, there is no way we can obtain the actual continuous function. The data taking routine with a fixed sampling rate can be presented as many delta functions evenly spaced in time as shown in the middle left panel, which is called the window function. The obtained data are discrete points sampled at each sampling time as shown in the bottom left panel. It is also the point-wise product of the underlying function and the window function. As the evolution theorem states, the FT of the obtained data shown in bottom right panel is equivalent to the convolution of the FT of the underlying continuous signal shown in top right panel and the FT of the window function shown in middle right panel. The FT of the obtained data is NEITHER the direct FT of the underlying continuous signal shown in Eq.5.2 NOR the top right panel. The FT of evenly-spaced delta functions as the window function is also delta functions evenly spaced proportional to the inverse of the time spacing shown in the middle two panels. As a result, the product of the two FTs has the window function imprinted on the FT of the underlying signal shown in the bottom right panel. Furthermore, the peak height presents the size of the frequency's component consistent with the peak in the Fourier transform of the signal source.

Mathematically, the obtained data is the point-wise product of the underlying signal and a set of delta functions, $g(t) \cdot III_{\Delta t}(t)$, where $g(t)$ is the signal and $III_{\Delta t}(t)$ is the observation points and the observation time is spaced by Δt. The FT of the data can be shown below in Eq.5.5 with applying the convolution theorem.

$$\mathcal{F}\{g(t)\cdot III_T(t)\} = \mathcal{F}\{g(t)\} * \mathcal{F}\{III_T(t)\} \tag{5.5}$$

$$= \sum_{-\infty}^{\infty} g(n\Delta t)\mathrm{e}^{-2\pi i f n\Delta t} \xrightarrow[\text{finite samples N}]{} \sum_{n=0}^{N} g_n \mathrm{e}^{-2\pi i f n\Delta t} \tag{5.6}$$

where $g_n \equiv g(n\Delta t)$, $III_{\Delta t}(t) = \sum_{n=-\infty}^{\infty} \delta(t - n\Delta t)$ and

$$\mathcal{F}\{III_{\Delta t}(t)\} = \frac{1}{\Delta t} III_{\frac{1}{\Delta t}}(f) = \frac{1}{\Delta t}\sum_{n=-\infty}^{\infty} \delta(f - n\frac{1}{\Delta t}) \tag{5.7}$$

The result is the discrete Fourier transform.

However, if the data is not evenly sampled in time as shown in the bottom left panel in Fig.5.4, the window function shown in the middle left panel in Fig.5.4 does not have an evenly-spaced delta functions like the one in the middle left panel in Fig.5.3. Its FT becomes many peaks at random places in frequency as shown in the right bottom panel in Fig.5.4. This FT of the window function imprinted on the actual signal randomizes the peaks originally in the FT of the signal. The largest peak in the FT of the obtained data no longer present as the largest frequency component in the signal. Therefore, the FT observed data does not produce a meaningful result if the time coordinate does not have data points evenly spaced.

Both the periodogram and the Fourier power spectrum are used to extract the power information of periodic signals. However, they are conceptually two different things. The Fourier power spectrum gives the actual power density of the underlying continuous signal within its frequency sensitive range for evenly-spaced data. But, if the data are not evenly-spaced, the FT fails and the periodogram only serves as a power estimator to look for possible periodic signals.

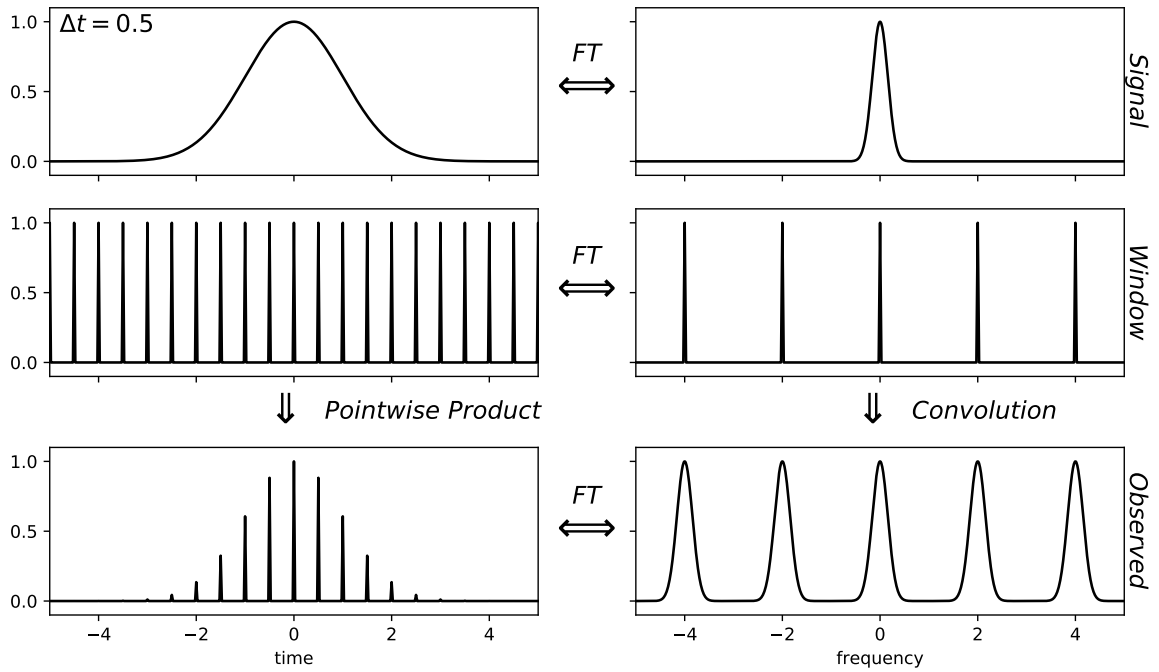

Figure 5.3: An illustration of convolution theory. The left top two panels are the underlying signal and the time coordinate of data taking. The left bottom panel is the actual observed data. The three panels on the right are the Fourier transforms of the functions on their left. The window function of the evenly-spaced data (middle right panel) gives delta functions spaced by $\frac{1}{cycle\,time}$. Therefore, the convolution of the FT of the underlying signal and the FT of time coordinate in the right bottom panel maintains the size of the peak in the FT of the underlying signal. Reproduced from Ref.[42]

5.3 The Lomb-Scargle periodogram and its extension

5.3.1 classical form

The classical periodogram, also called Schuster periodogram, has the same form as the Fourier power spectrum besides a normalization factor $\frac{1}{N}$, where N is the number of data points. The discrete Fourier transform of a sampled data set, $\{g_n = g(t_n), n = 1, 2, , ..., N\}$, can be shown as $\mathcal{F}\{g_n\}$. The classical form is defined as:

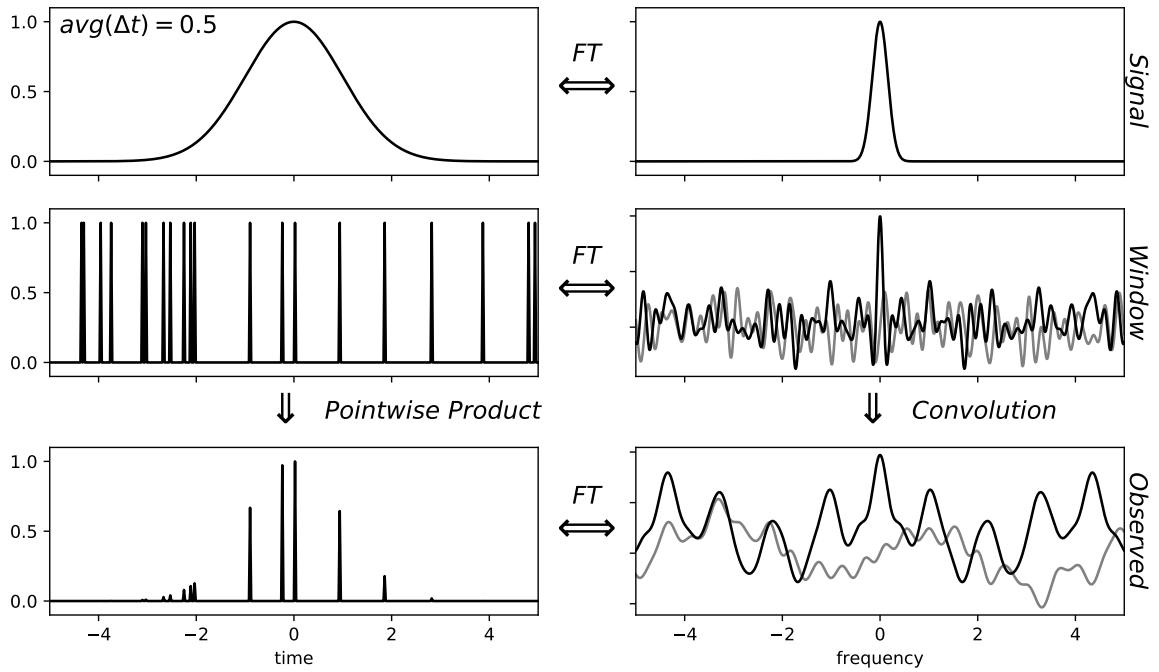

Figure 5.4: An illustration of convolution theory. The left top two panels are the underlying signal and the time coordinate of data taking. The left bottom panel is the actual observed data. The three panels on the right are the Fourier transforms of the functions on their left. The window function of the unevenly-spaced data (middle right panel) gives peaks at random frequency locations. The convolution of the FT of the underlying signal and the FT of the time coordinate in the right bottom panel fails to present the frequency information of the underlying signal. Reproduced from Ref.[42]

$$\mathcal{P}(f) = \frac{1}{N}\left|\mathcal{F}\{g_n\}\right|^2 \tag{5.8}$$

$$= \frac{1}{N}\left|\sum_{j=1}^{N} g_n \mathrm{e}^{-2\pi i f t_n}\right|^2 \tag{5.9}$$

$$= \frac{1}{N}\left[\Big(\sum_n g_n \cos(2\pi f t_n)\Big)^2 + \Big(\sum_n g_n \sin(2\pi f t_n)\Big)^2\right] \tag{5.10}$$

The classical form ignores data not being evenly spaced. The real peaks in the spectrum give rise to many other peaks of various heights across the spectrum as the case shown in

the bottom right panel in Fig.5.4. It works beautifully with evenly-spaced data but has no well-defined properties for others. Scargle[37] pointed out that researchers had moved away from this method and categorized its problems into two: statistical difficulties and spectral leakage. The main statistical problem is the spectrum is very noisy no matter how many data points there are. Increasing the number of data points also adds the number of available frequencies in proportion so the noise does not get averaged out. The second issue, spectral leakage, is adopted from the frequency analysis with the number of data being finite. For a sinusoidal signal with a single frequency, its classical periodogram has a peak not only at the correct frequency but also at other frequencies.

There are different methods to analyze unevenly-spaced data. Each method can also have several slightly different forms such as the way of normalizing the periodogram. It leads to different statistical properties.

5.3.2 L-S periodogram

The L-S periodogram is inspired by Fourier analysis and modified with the concept of least-squares frequency analysis. Therefore, the standard form has some similarities with the Fourier power spectrum. It can be partially derived with a Fourier analysis approach[37] and fully derived with a least-squares frequency analysis approach[28][45]. Here I want to briefly explain how to obtain the standard form with Least-squares frequency analysis.

The core concept of the least squares method is to find the best model to represent the actual data by minimizing the difference between the two. The intuitive model for a simple periodic signal with a single frequency is a linear combination of sine and cosine functions. For each frequency, theoretically we can obtain the coefficients of the sine and cosine functions as a function of frequency by minimizing the sum of squares. Then, we can construct a periodogram as a collection of the sums of squares as a function of frequency. The smaller the peak is, the better fit the model presents. However, the calculation is not trivial. Lomb keeps the core concept of the least squares method by minimizing the sum of squares: $\sum_{n=1}^{N} \left[g(t_n) - g_f(t_n)\right]^2$ where $g(t_n)$ is the actual data and $g_f(t_n)$ is the model you

are fitting to. Instead, Lomb constructs a periodogram as a set of quantities which shows how well the models represents the actual dataset, not the chi-square value directly. The greater the value is, the closer the model is to the actual data. This quantity extracts the magnitude of the specified frequency's component in the model that the actual data also obtain. It can be thought of as a dot product of two vectors pointing in two directions[44]. One vector is the data and another one is the unique solution in the model that minimizes the sum of squares. And the dot product extracts the component of the data vector parallel to the solution vector. If the model can describe the data well, the dot product of the two gives a value close to 1 with the proper normalization.

Also Lomb implements a time shift, τ, in the time base which makes the periodogram invariant under a global time shift. On the other hand, mathematically, this constant, τ, greatly simplifies the calculation to obtain the coefficients of the sine and cosine functions in the model by just adding a phase in the functions without changing the solution.

The Lomb-Scargle peridogram can be shown as the form:

$$\mathcal{P}(f) = \frac{A^2}{2}\Big(\sum_n g_n \cos(2\pi f[t_n - \tau])\Big)^2 + \frac{B^2}{2}\Big(\sum_n g_n \sin(2\pi f[t_n - \tau])\Big)^2 \tag{5.11}$$

This form has lots of similarities to the classical form in Eq.5.8. A, B and τ are arbitrary function of the frequency f.

Plugging in A, B and τ, the Lomb-Scargle periodogram without any normalization has the form:

$$\mathcal{P}_{\mathcal{LS}}(f) = \frac{1}{2}\left\{\frac{\Big(\sum_n g_n \cos(2\pi f[t_n - \tau])\Big)^2}{\sum_n \cos(2\pi f[t_n - \tau])} + \frac{\Big(\sum_n g_n \sin(2\pi f[t_n - \tau])\Big)^2}{\sum_n \sin^2(2\pi f[t_n - \tau])}\right\} \tag{5.12}$$

where the τ is specified for each frequency f to ensure time-shift invariance:

$$\tau = \frac{1}{4\pi f}\tan^{-1}\Big(\frac{\sum_n \sin(4\pi f t_n)}{\sum_n \cos(4\pi f t_n)}\Big) \tag{5.13}$$

Eq.5.12 can be normalized with a factor of $\frac{1}{\sum g_n^2}$.

5.3.3 Modifications of L-S periodogram

Lomb-Scargle periodogram shown in Eq.5.12 has two drawbacks. First, it does not include the error bars of the data in the analysis. Gilliland and Baliunas[19] and Irwin et al.[26] first provided a version of the modified L-S periodogram for the unequally weighted data. Scargle[38] also included the form of a periodogram for data with uneven weights. The second drawback is the L-S periodogram assumes the data has pre-centered so that the mean of the data and the mean of the fitted sine function are the same. Its modification has been called various names: the data-compensated discrete Fourier transform by Ferraz-Mello[17], the floating-mean periodogram by Cumming et al.[12] and VanderPlas and Ivezic 2015[43]), and the generalized Lomb-Scargle periodogram by Zechmeister and Kurster[45]. Mainly, it adds an offset term in the fitted model at each frequency. It is not equivalent to subtracting the mean from the signal to remove the signal offset. It is because the signal most likely does not have the full phase coverage on the observed measurement. Removing the mean might suppress periodic signals in the periodogram. VanderPlas[42] has shown an example on this case.

These two are the most important modifications of L-S periodogram. Zechmeister and Kurster have derived the modified L-S periodogram in detail. With a sampled data set, $\{g_n, n = 1, 2, .., N\}$ with the corresponding uncertainties, $\{\sigma_n\}$, the L-S peridogram with uneven weighting can be presented as:

$$\mathcal{P}_{\mathcal{LS}}(f) = \frac{1}{\sum w_n (g_n - \overline{g})^2} \left\{ \frac{\left(\sum w_n (g_n - \overline{g}) \cos(2\pi f[t_n - \tau]) \right)^2}{\sum w_n \cos^2(2\pi f[t_n - \tau]) - \sum w_n \cos(2\pi f[t_n - \tau]) \cdot \sum w_n \cos(2\pi f[t_n - \tau])} \right.$$
$$\left. + \frac{\left(\sum w_n (g_n - \overline{g}) \sin(2\pi f[t_n - \tau]) \right)^2}{\sum w_n \sin^2(2\pi f[t_n - \tau]) - \sum w_n \sin(2\pi f[t_n - \tau]) \cdot \sum w_n \sin(2\pi f[t_n - \tau])} \right\} \quad (5.14)$$

where $\overline{g}$ is the weighted mean and w_n is the weight of each measurement and w_n is normalized with the total weight, W, as shown below.

$$\overline{g} = \sum w_n g_n \tag{5.15}$$

$$w_n = \frac{1}{W}\frac{1}{\sigma_n^2} \qquad \left(W = \sum \frac{1}{\sigma_n^2} \qquad \sum w_n = 1\right) \tag{5.16}$$

5.3.4 Normalization

The L-S periodogram is inspired by Fourier analysis and also can be viewed as a special case of Least Squares method. These two perspectives have slightly different interpretations on what the periodogram is measuring. Here I will introduce two commonly-used normalizations: PSD normalization and Least-Squares normalization.

Eq.5.12 itself without an additional normalization factor, $\frac{1}{\sum g_n^2}$, is the resulting periodogram in the Fourier perspective for the case of no measurement uncertainty included. It outputs the standard Fourier power spectrum for the special case of evenly spaced data. It is called the PSD normalized periodogram or unnormalized L-S periodogram. It can also be expressed in Least-Squares language as:

$$\mathcal{P}(f) = \frac{1}{2}[\hat{\chi_0}^2 - \hat{\chi}^2(f)] \tag{5.17}$$

$\hat{\chi_0}^2$ is the non-varying reference model. For the case of Eq.5.12 without measurement uncertainties, $\hat{\chi_0}^2 = \sum (g_n)^2$. And $\hat{\chi_0}^2 = W \sum w_n (g_n - \overline{g})^2$ for the case of Eq.5.14 with considering floating-mean value and uneven weighting.

For the evenly spaced data, Eq.5.17 is consistent with the result of the Discrete Fourier power spectrum with N data points: $\frac{1}{N}\left|\mathcal{FFT}(g_n)\right|^2$.

Without considering the data uncertainties, the unit of the periodogram is $\mathcal{O}[g^2]$ and it measures the squared-amplitudes of Fourier components at each frequency. With the uncertainties, its unit is unitless and it measures the periodic signal in signal-to-noise ratio.

Eq.5.12 with the normalization, $\frac{1}{\sum (g_n)^2}$, is the periodogram with least-squares normalization. It measures the inverse of the goodness-of-fit for a model. The expression in Least-

squares language is:

$$\mathcal{P}(f) = \frac{\hat{\chi_0}^2 - \hat{\chi}^2(f)}{\hat{\chi_0}^2} \tag{5.18}$$

$\hat{\chi}^2(f)$ describes the fit between the actual data and the model. When the model perfectly fits to the data, $\hat{\chi}^2(f)$ is zero then $\mathcal{P}(f)$ is equal to 1. For other cases, the $\hat{\chi}^2(f)$ is greater than zero and $\mathcal{P}(f)$ lies between 0 and 1. This normalization gives a value proportional to the result of an unnormalized peridogram. The unit of the least-squares peroidogram is dimensionless.

There are more than two normalizations of the L-S periodogram but they are barely used in the literature. Different normalizations can have different statistics of the resulting periodogram when interpreting the significance of the peak. Baluev[7] has a summary on normalization and its statistical properties.

5.4 The interpretation on peaks

In my experience of analyzing unevenly-spaced data, I encountered one important concept of the periodogram after learning the basic knowledge. That is how to interpret the peaks in the periodogram. Without it, it is meaningless to calculate the periodogram. The statistics of the periodogram gives us more insight to obtaining various size of peaks. Before jumping into the core, it is good to know how the peridogram with different normalization can have different statistical properties.

The periodogram and Fourier power spectrum have very different information about periodicity of the signal so they have very different ways to interpret the peaks. In a Fourier power spectrum, the width of the peak is an important quantity because it determines the uncertainty of the frequency you detect. It decreases with the number of data points and signal-to-noise ratio. However, the width of a peak in periodogram does not depend on these two parameters. More than that, periodogram is not about how precise you can determine the frequency in the data but, as power estimators at each frequency, how unlikely the largest peak with such magnitude is caused by noise fluctuation. A good quality of data

in the periodogram reflect on how distinguished the height of the peak from others caused by noise. This quantity is false alarm probability(FAP). It is based on a null hypothesis to assume no periodic signal but only white Gaussian noise exist in data and estimates the probability the peak in the periodogram is caused by the noise. A larger peak leads to a smaller value of FAP which corresponds to a smaller value of significant level. The smaller the significance level is, the more unlikely it is caused by just noise.

5.4.1 Statistics of the L-S periodogram

For even-sampled data, the powers at different frequencies in the Fourier power spectrum have a well known statistical distribution. If the signal is white Gaussian noise, the histogram of the power gives a chi-squared distribution with two degrees of freedom which is an exponential probability distribution. For the case of unevenly spaced data, Scargle shows the spectral estimator at one frequency in the unnormalized L-S periodogram in Eq.5.12 gives the same exponential probability distribution. It can be useful because for certain instances it gives information about the significance level of peaks.

Scargle derived the result by starting with a generalized discrete Fourier transform(DFT) with a preselcted frequency, f. Its periodogram power has an exponential probability distribution if the source signal is independently and normally distributed data with zero mean and constant variance[37]. A generalized DFT of a set of N data points with the sampling, $\{t_n\}$,can be shown as

$$FT_g(f) = \frac{1}{N^2}\sum_{n=1}^{N} g_n\Big[Acos(2\pi f t_n) + iBsin(2\pi f t_n)\Big] \tag{5.19}$$

A and B are unspecified functions of f. The corresponding periodogram of the DFT is:

$$
\begin{aligned}
P_{DFT}(f) &= \frac{1}{N}|FT_g(f)|^2 \\
&= \frac{A^2}{2}\Big[\sum_n g_n cos(2\pi f t_n\Big]^2 + \frac{B^2}{2}\Big[\sum_n g_n \sin(2\pi f t_n)\Big]^2 \\
&= \frac{1}{2}\Big[C^2(f) + S^2(f)\Big]
\end{aligned}
\tag{5.20}
$$

where $C(f) = A\sum_n g_n \cos(2\pi f t_n)$ and $S(f) = B\sum_n g_n \sin(2\pi f t_n)$. The result is under the assumption that $C(f)$ and $S(f)$ are uncorrelated.

As shown in Eq.5.20, the periodogram can be generalized as the sum of the squares of two normally distributed, zero-mean random variables with the same variance so it is by definition a chi-squared distribution with two degrees of freedom which is an exponential probability distribution[29]. Let X and Y be two zero-mean random variables with variances, σ_X^2 and σ_Y^2 and $\sigma_X^2 = \sigma_Y^2 = \sigma^2$. Papoulis[29] derived that $Z = X^2 + Y^2$ has the exponential distribution:

$$
P_Z(z) = \frac{1}{2\sigma}\mathrm{e}^{-z/2\sigma^2} \tag{5.21}
$$

where z is the power in L-S periodogram, P_{LS}[37]. As a result, with only the pure Gaussian noise as signal, powers at each frequency in the periodogram have an exponential probability distribution. The spectral estimator of a sampled data set, $\{g_n = g(t_n), n = 1, 2, , ..., N\}$, at a given frequency, f_0, is $Z_0 = P_g(f_0)$ in the unnormalized L-S periodogram, the probability of obtaining a peak larger than Z_0 is e^{-Z_0} and the probability of obtaining a peak less than Z_0 is $(1 - \mathrm{e}^{-Z_0})$. The probability of obtaining a peak greater than the value Z_0 decreases as e^{-Z_0} with an increased Z_0. This value is directly useful if the signal at this frequency is the only one of interest. However, most of cases, we are more interested in the largest peak in a range of frequencies. And we want to be able to know what is the probability of obtaining this peak if there is no actual periodic signal in the data. It requires us to examine the height of the spectral estimator at each frequency in the range. Assuming the spectral estimators at each frequency are independent from each other, for a simple case of

only three frequencies in the range, the probability of obtaining a peak greater than Z_0 in all three frequencies is $e^{-Z_0} * e^{-Z_0} * e^{-Z_0}$ which is extreme small. But, the probability that the largest peak among these three frequencies is greater than Z is (1−Prob[*none of them obtains a peak greater than* Z_0]). That is $1 - (1 - e^{-Z_0})^3$. However, the assumption is not realistic. Sampling time being unevenly spaced causes the values at different frequencies to correlate with one another. There are various approach to estimate the effective independent number of frequencies, N_{eff}, and the FAP is shown as:

$$Prob[Z_{max} > Z] = 1 - [1 - exp(-Z)]^{N_{eff}} \tag{5.22}$$

Because of the survey window function, it is not a trivial task to determine the N_{eff}. Horne and Baliunas[25], Cumming[11], and Frescura et al.[18] has proposed ways to estimate this value but they are all just approximations.

5.4.2 Bootstrap

Another approach to estimate FAP is the bootstrap method. It estimates the statistic of the periodogram from the statistic of the bootstrap samples' periodograms. In the oscillating EDM analysis, FAP of the largest peak in the periodogram is estimated by comparing with the distribution of the maximum peak's magnitude from the periodograms of the bootstrap samples. To contain a similar noise level and wash out any possible periodic signal to satisfy the assumption of Null hypothesis, the bootstrap sample is consisted with points that are randomly drawn with replacement from the original dataset such that some values can appear more than once in the bootstrap sample. The time coordinate is kept the same so the maximum peak distribution has taken the survey window into account. By collecting the magnitude of largest peak from the periodogram of each bootstrap sample, we can obtain the maximum peak's magnitude distribution of the bootstrap sample's periodogram. Depending on where the largest periodogram peak of the actual dataset fall in the distribution, it gives the probability of obtaining the peak with such a magnitude in the expected maximum peak's

magnitude probability distribution which is the FAP of the peak.

Bootstrap was first proposed by Efron in 1979[15]. And it is believed to be a better and more primitive way to estimate the FAP than N_{eff} method mentioned in section 5.4.1 because of three reasons. First of all, it has fewer assumptions on the form of periodogram probability distribution than the N_{eff} method does. Second, it has accounted for the effect of the survey window with keeping the same time coordinate in resampled data. And third, the N_{eff} method tends to under-estimate the FAP and still has an unambiguous issue on determining N_{eff}. Jacob[42] has compared the result of FAPs from several methods including N_{eff} and bootstrap. The drawback of bootstrap is the computation cost could be high especially for the case of very small value of FAP. Also, the application of the bootstrap method on the correlated signal can be very complicated, see [27].

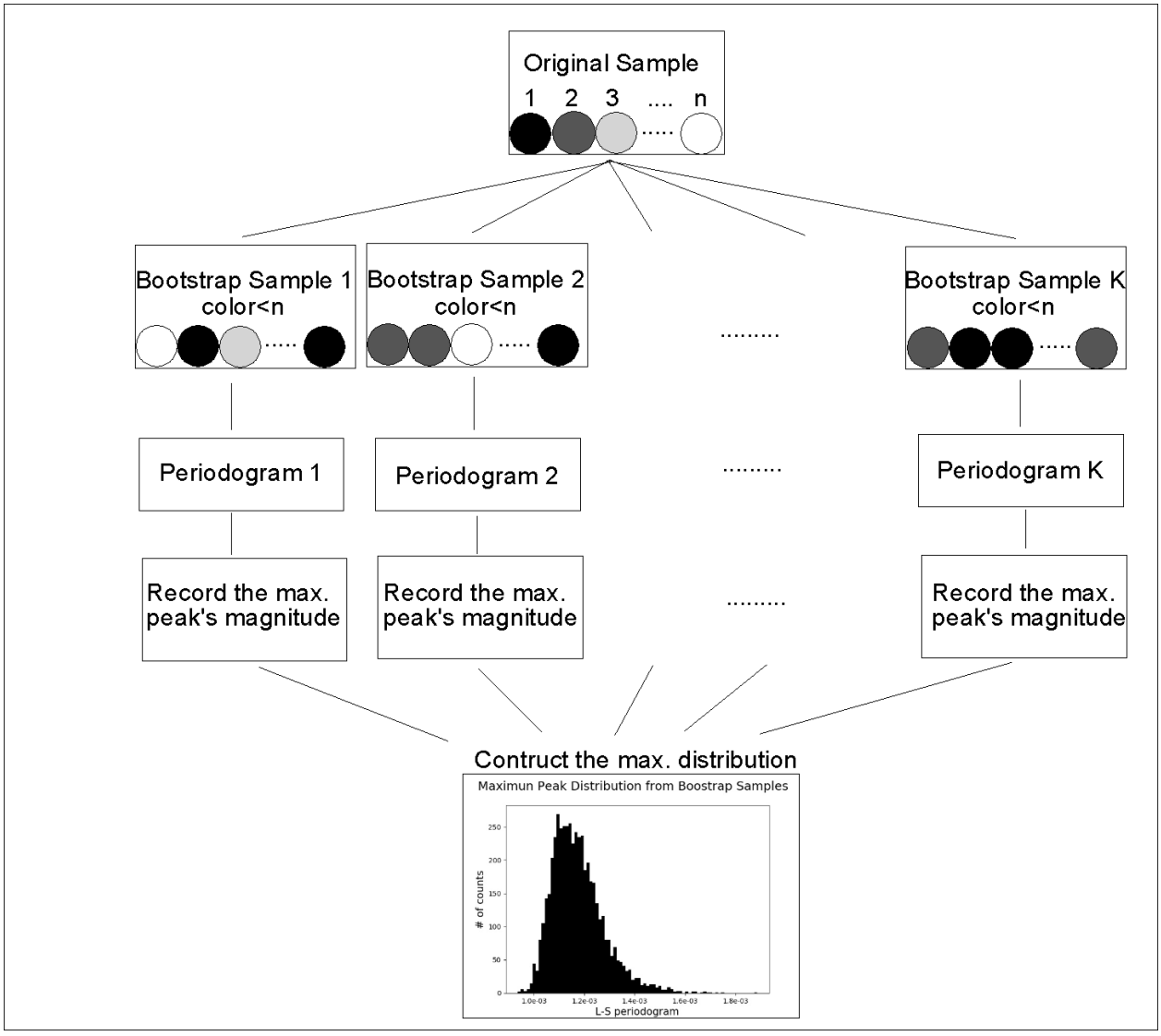

Figure 5.5: An illustration of bootstrap method. The original data points can be thought of as n balls with n different colors shown in the top of illustration. The bootstrap samples are consisted with the points that are drawn randomly with replacement from the original data set. It allows the same data point can be drawn more than once. Therefore, the bootstrap samples are expected to have n balls with the number of colors less than n, what the original data has.

Chapter 6

DATA ANALYSIS

This chapter first discusses the two important procedures while applying the L-S periodogram on EDM data and then presents our result of the L-S periodogram analysis and the sensitivity of our measurements. First of all, EDM data cannot directly be analyzed because the EDM string points are not independent. Also, the Nyquist limit of EDM data is well defined because it is very nearly evenly spaced. It is also reflected in the window power spectrum.

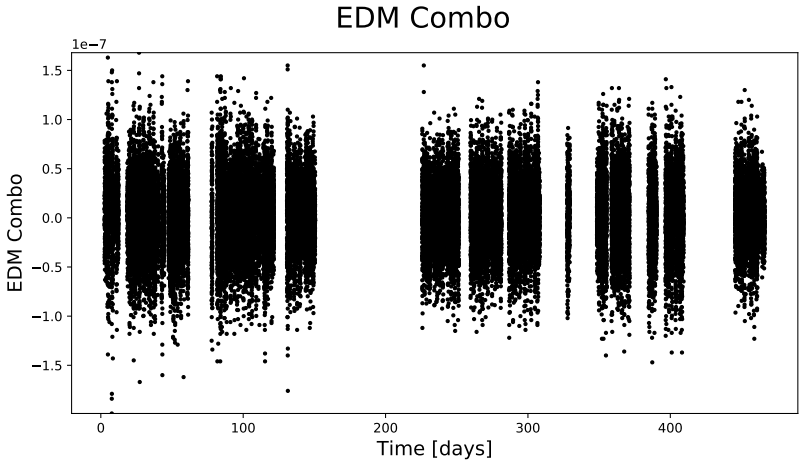

Figure 6.1: EDM measurements combining HV settings of 6kV and 10kV verse time. 6kV data has scaled by 10/6. Measurements are mostly equally spaced in time except the large gaps where the experiments are paused for maintenance.

Figure 6.1 is the static ^{199}Hg EDM data. There are 52,695 data points over 284 completed days. They are EDM values after applying the string analysis mentioned in earlier chapters. The sensitivity of the static EDM measurement is proportional to the high voltage applied across the middle two cells. For the systematic analysis purpose, we switch the HV setting

between 6kV and 10kV frequently. As a result, the data with 6kV scatters about $\frac{10}{6}$ more than the data with 10kV. In Fig.6.1, the 6kV data has been scaled by $\frac{10}{6}$ to combine with 10kV data. For searching for a time-varying EDM, these 52,695 data points are either error weighted without 6kV data rescaling or weighted equally with 6kV data rescaled in the periodogram analysis. The error of each data point is calculated by the scatter of the data points in that night. During the data taking, the measurements are mostly equally spaced by the cycle time between 270 seconds to 285 seconds. The gaps between points in Fig.6.1 are the times we paused the experiment every morning for the apparatus maintenance, configuration setup, or fixing the apparatus.

6.1 Facts

6.1.1 EDM data being not independent

The static EDM data cannot be directly interpreted in the frequency domain through the Lomb-Scargle periodogram for searching an oscillating EDM because the string analysis, mentioned in the section 4.2, takes the linear combination of three neighboring EDM points to remove the time-dependent linear field gradient drift. Therefore, all the EDM string points are not independent and the noise are not Gaussian white noise. If directly calculating the L-S periodogram on the EDM string points, the result has an overall $\frac{1}{f}$ structure as shown in Figure 6.2.

Figure 6.3 shows the results of the Lomb-Scargle periodogram both from the Gaussian distributed independent data in the upper panel and the data after applying string analysis in the middle panel. Both data sets are assigned with the time array as the one of EDM data and points are evenly weighted. The upper figure shows peaks spreading across the whole frequency range without obvious structure. However, the L-S periodogram of the data after string analysis has a spectrum with a $\frac{1}{f}$ structure. The high frequency signals are suppressed from the string analysis which averaging every three neighboring raw points. Because the periodogram is normalized by the standard deviation of the data, the low frequency signals

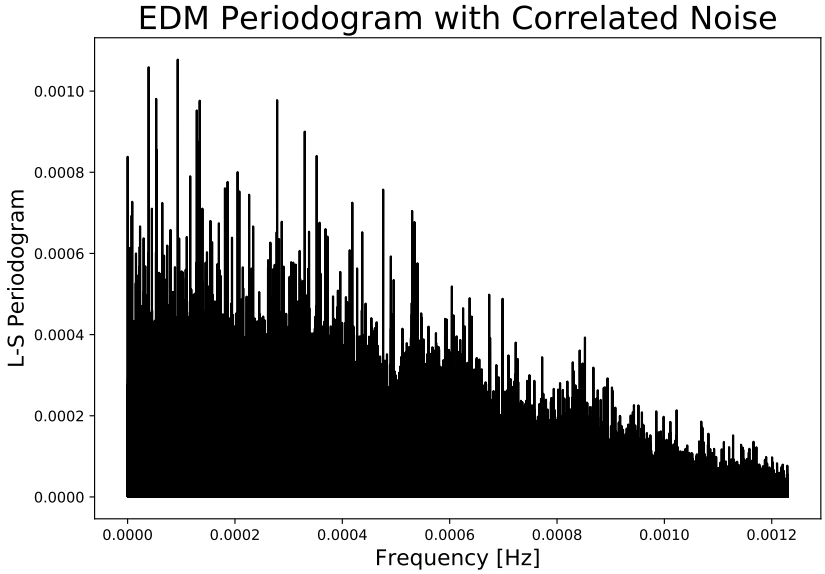

Figure 6.2: The EDM periodogram from the correlated EDM data. The overall 1/f shape is due to the string analysis.

have bigger amplitudes than the one in the upper panel.

Instead of analyzing the correlated string points directly, I split the data points to three groups such that the first(second and third) group contains the first(second and third) string point and every other two points in the data set. Therefore, all the points in each group are independent. Then, the final periodogram is the average of the three periodograms from the three groups. Each periodogram is calculated with standard normalization so it has the form of $1 - \frac{\hat{\chi}^2(f)}{\hat{\chi_0}^2}$ as mentioned in Eq.5.15. Coming from the same data source, $\hat{\chi_0}^2$ from each group is expected to be the same. Therefore, it is reasonable to take the average of the power estimators at the same frequency from three groups to get the final power estimator at that frequency. Repeating it for all the frequencies, we can obtain the final periodogram. This is the method we are using to detect the oscillating EDM with the static EDM data.

Applying it on the simulated data set in the middle panel in Fig.6.3, the final periodogram does not have the $\frac{1}{f}$ structure as shown in the bottom panel. The periodogram becomes three

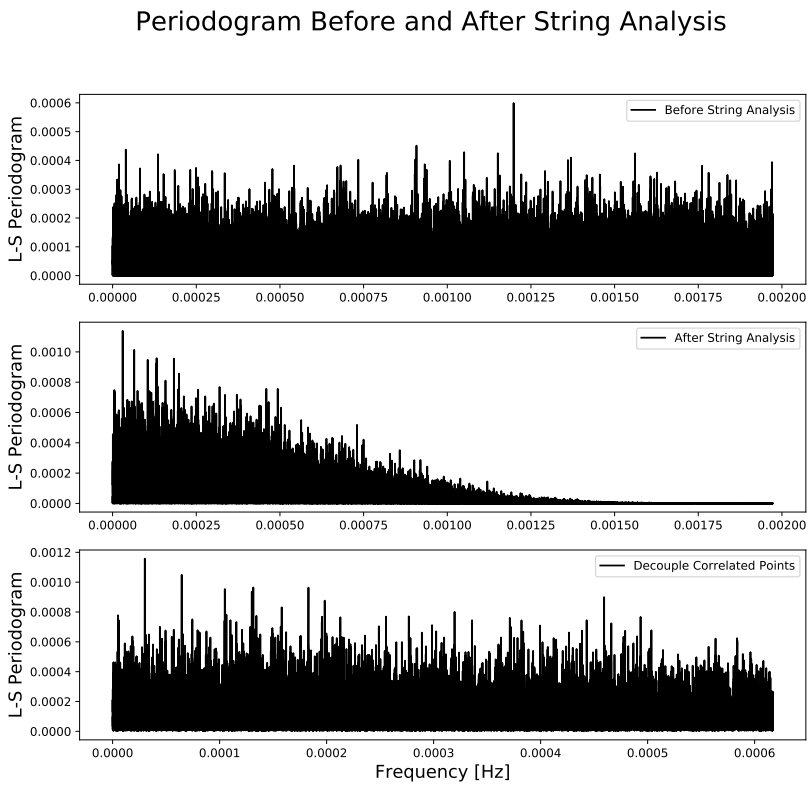

Figure 6.3: The periodograms before(top panel) and after(middle panel) the string analysis on a simulated Gaussian-distributed data. The overall 1/f shape in frequency is caused by the string analysis. By decoupling the correlation among data points in the middle panel, the frequency range of the final periodogram(bottom panel) is shorten by a factor of three.

times shorter than before which will be discussed in section 6.1.2.

6.1.2 Effective Nyquist frequency and window function

The regularly-sampled data has a well-defined Nyquist limit due to the symmetry in its Dirac comb window function. The uneven spacing of the samples randomize the locations of the peaks in the Fourier transform. As a result, it does not always have a Nyquist limit. Even if it does, normally the Nyquist limit is larger than the case of evenly-spaced data[43]. For the static EDM measurement, the observations are nearly equally-spaced. Each EDM value

is calculated from the neighboring cycles with the string analysis and each cycle has a fixed length between 240 seconds and 300 seconds in that day. Figure 6.4 shows number counts for various intervals between the observations. The most common setup is 270 seconds for a cycle time. As a result, the window function has clear peaks spaced by 1.23×10^{-3} Hz which is equal to the inverse of three cycle times, $\frac{1}{3\times270}$, shown in the upper panel in Fig.6.5. The factor of 3 is due to the step of decoupling the correlation between neighboring points mentioned in section 6.1.1. If the data was perfectly evenly-spaced, the peaks would be many delta functions with larger magnitude and without any additional small peaks besides it as in the bottom-right panel in Fig.5.3. Because of the nearly equally-spaced observation, we can treat $f_{Ny} = \frac{0.5}{3\times270} = 6.17 \times 10^{-4}$ Hz as the effective Nyquist limit for the oscillating EDM analysis.

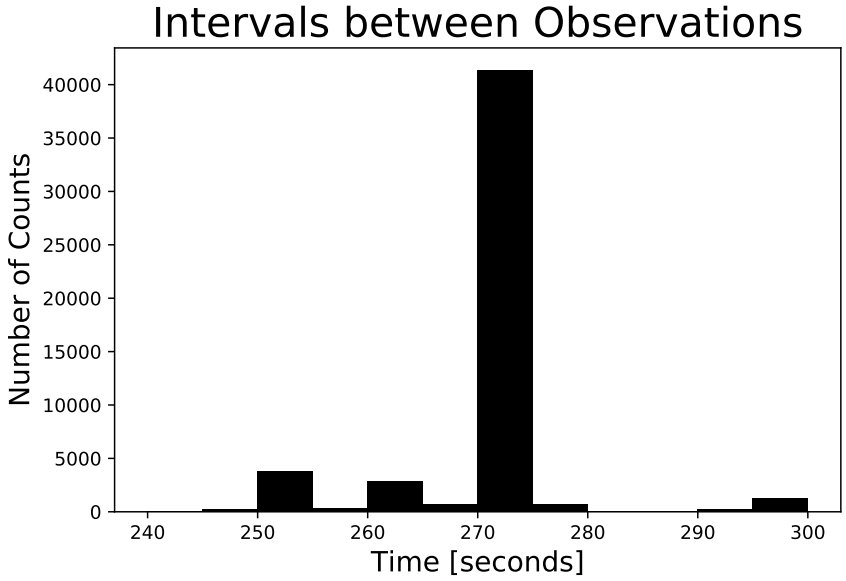

Figure 6.4: A histogram of EDM cycle time. EDM data are mostly evenly spaced in time and the most common setup for a cycle time is 270 seconds.

By injecting a periodic signal with a large amplitude into the EDM data, the periodogram shows the fake signal's folded peaks at the position mirrored about the effective Nyquist

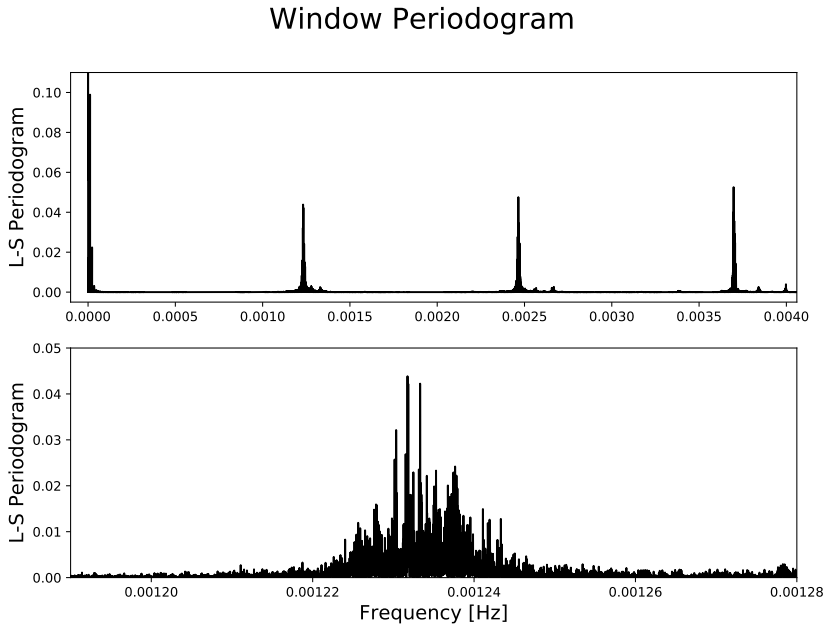

Figure 6.5: The window function of EDM data. Because the data are mostly evenly spaced in time, so the window function(top panel) has clear peaks spaced by $\frac{1}{3\times cycle\,time}$, where the three is due to decoupling the correlation among data. An enlarged look(bottom panel) on the structure of one of the peaks.

frequency, 6.17×10^{-4} Hz, shown in Fig.6.6. The dash lines indicate the frequencies at 6.17×10^{-4} Hz, $2 \times 6.17 \times 10^{-4}$ Hz, $3 \times 6.17 \times 10^{-4}$ Hz, and $4 \times 6.17 \times 10^{-4}$ Hz.

6.2 Oscillating EDM result

The EDM data set has a total of 52,697 string points over 284 completed days. I analyze the data with two different approaches both with and without error weighting shown in Fig.6.7. The first approach, the Combined HV Periodogram, is to split the data to three groups first so all the points in the group are totally independent from each other. The final periodogram is the average of these three sets' periodograms shown in the left panel in Fig.6.8 and in Fig.6.10 for the cases with and without error weighting. As mentioned earlier in this chapter, because 6kV data is expected to scatter about $\frac{10}{6}$ more than the 10kV data,

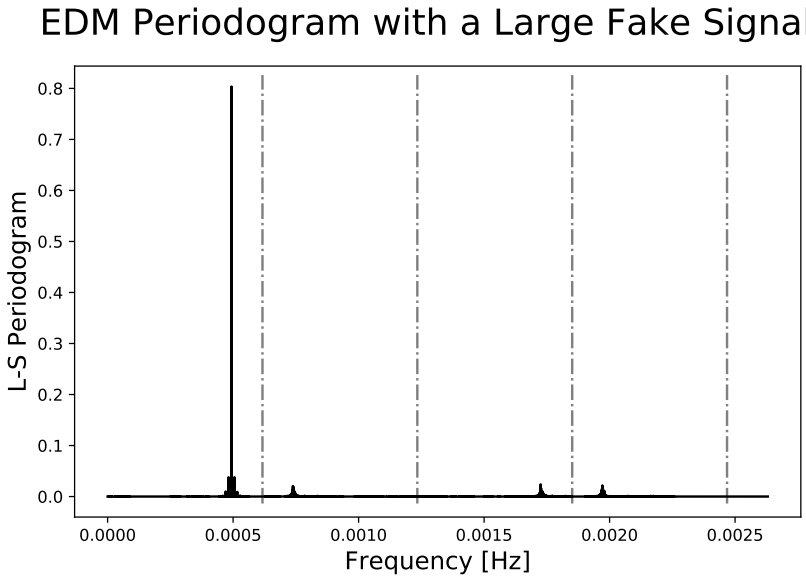

Figure 6.6: The window function with an injected large signal at 4.9×10^{-4} Hz. The mirrored peaks indicate the effective Nyquist frequency:6.17×10^{-4} Hz

it is rescaled by $\frac{10}{6}$ in the case of the Combined HV Periodogram without error weighting. The error weighted Combined HV Peridogram does not need to rescale 6kV data because the size of scattering is taken into account with error weighting.

Because the EDM data scatter with HV value and the EDM data taking sequence switches HV setting between 6kV and 10kV every other day, it could act like a time varying signal. Therefore, another approach to obtain the final result on the periodogram, called 2HV Periodogram and shown in the bottom panel in Fig.6.7, is to separate 6kV and 10kV data first and calculate their individual periodogram by averaging the three split data sets' periodogram as shown in Fig.6.9 and then take the average of these two results to obtain the final periodogram shown in the right panel of in Fig.6.8 and Fig.6.10 for the cases with and without error weighting. Because 6kV and 10kV data are separated first before calculating the periodogram, there is no need to rescale 6kV data.

The measurement is sensitive in the frequency range from 0 Hz to 6.17×10^{-4} Hz as explained in the section 6.1.2. The frequency grid is suggested to over-sample the peak with

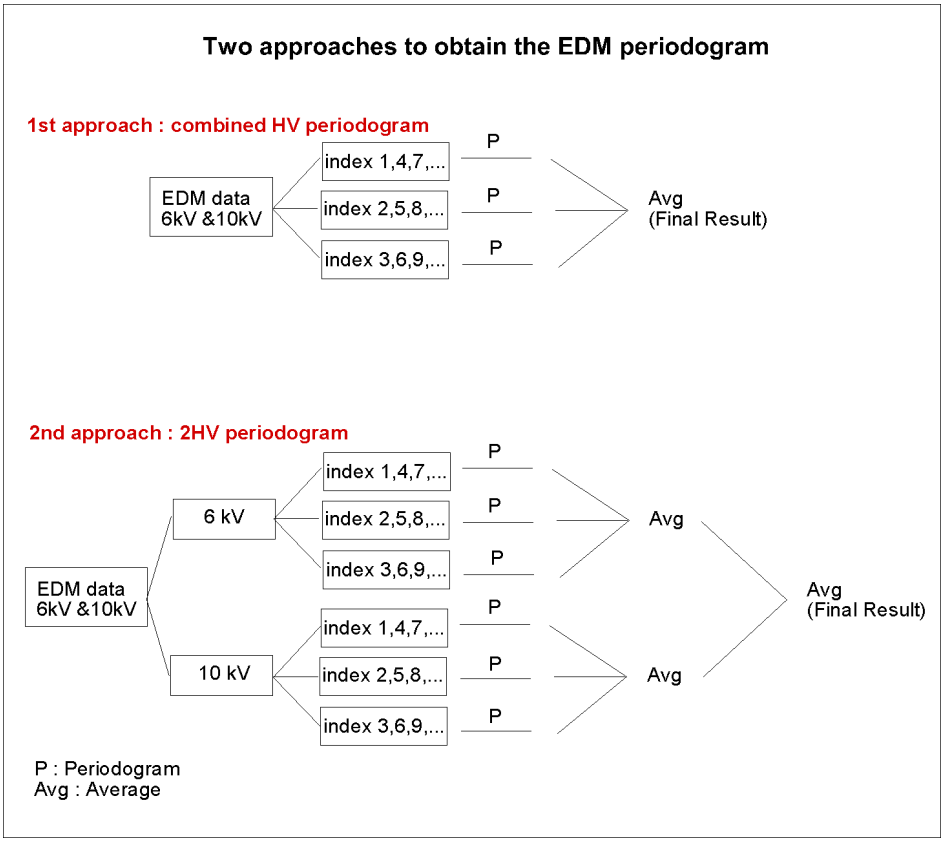

Figure 6.7: An illustration on the two approaches to obtain the final periodogram.

expected width by a factor of 5[40][43] to 10[13][33] so that each peak has 5 to 10 samples. In the oscillating EDM analysis, there is no information about the potential signal's width so I use the inverse of the total time length, ∼15.45 months, as the peak's width and an oversampling factor of 5 makes a frequency grid to be $\frac{1}{5\times 15.45\, month} = 4.99 \times 10^{-9}$ Hz.

There are a total of four periodograms calculated from two approaches with and without error weighting shown in Fig.6.8 and Fig.6.10. The two dashed lines in the plots are the significance levels corresponding to the maximum peak's FAP of 5% and .3%. The most significant peak among four periodograms has a FAP of 31% at 3.92×10^{-5} Hz with a magnitude of 1.11×10^{-3} in the error weighted Combined HV Peridogram. It says this peak with such a magnitude, assuming no periodic signal in the dataset, has 31% probability to

be caused by noise. The common mistake is to interpret it as a 69% probability ro be caused by a periodic signal regardless of the calculation on FAP being based on the assumption of no periodic signal. Therefore, I claim the four periodograms are consistent and detect no periodic signal with a significant value in the periodograms.

The FAP, more specifically called the FAP of the maximum peak, is only relevant to the magnitude of the maximum peak in the peridogoram here. The FAP is determined by comparing the size of the maximum peak in EDM periodogram with the the maximum peak distribution of bootstrap samples' periodograms using the bootstrap method. For EDM data, we construct 1,000 periodograms from resampling the original data as explained in section 5.4.2. Each data point in bootstrap sample is randomly drawn with replacement from the original set so any points in the original data set can be picked more than once. The maximum distribution consists of 1,000 magnitudes of the maximum peak of each periodogram. As the first approach, the Combined HV periodogram, being the average of three, these 1,000 periodograms are also the averaged periodogram of the three. The EDM data is split to three groups first and then the points in three resampled data sets are randomly picked from these three groups separately but with the same corresponding order in the split group among the three groups. After calculating the L-S periodogram of these three resampled data sets and taking the average of the three periodograms, we can obtain one maximum peak magnitude of the averaged periodogram. Repeating it with different resampling combinations 1,000 times gives us the maximum peak distribution.

For the second approach of the EDM periodogram, the 2HV peridogram, the bootstrap method is also used to generate the maximum peak distribution. Because the 2HV peridogram is the average of the 6kV and 10kV periodograms, the procedure of constructing the maximum peak distribution has to be slightly altered such that the 6kV data and 10kV data are separated before splitting to three groups and each maximum peak is from the averaged periodogram of 6kV and 10kV periodogram of the resampled data.

A small subtilty in generating bootstrap samples in my analysis is to bootstrap each night of data separately and independently from other nights of data after splitting to three

groups. And then, I combine all the bootstrap samples from each night to calculate the L-S peridogram of one group. It is because each night's data has a slightly different distribution from each other. Some nights might scatter more than another night. It can be seen in the histograms of each night of 6kV data in the first group shown in the right panel of Fig.6.11. The left panel in Fig.6.11 shows the histogram of the first group of all the 6kV data in a logarithmic scale. The distribution of the data fits to a Gaussian function as shown in blue line very well. The data value has the unit of angular frequency per 10 kV electric field strength before converting to EDM unit:$e \cdot cm$. The conversion factor is 1.648×10^{-25}. And all the data still have a common blind offset so the mean value of the fit is not meaningful here.

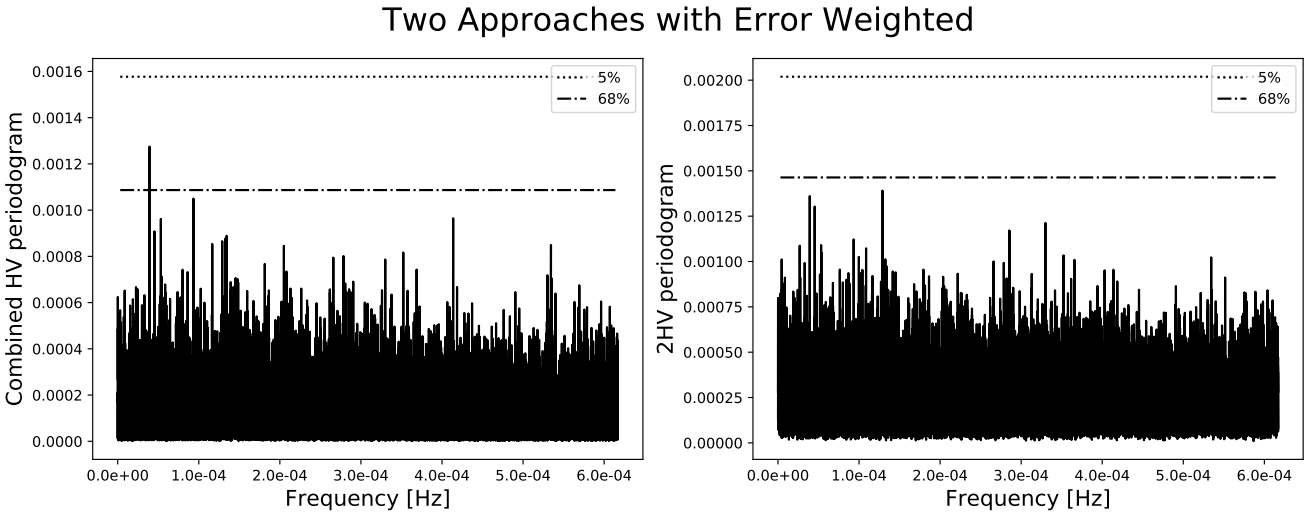

Figure 6.8: EDM periodograms with error weighted. The left panel is the Combined HV peridogoram with the maximum peak at 3.92×10^{-5} Hz with the FAP of 31%. The right panel is the 2HV peridogoram with the maximum peak at 1.29×10^{-4} Hz with the FAP of 82%. The horizontal lines are the FAP of the maximum peak at 5% and 0.3%.

The sensitivity of our measurement with 95% confidence is defined as the smallest periodic signal which can be detected as the maximum peak with 95% probability. It is determined by injecting a fake signal in the resampled data constructed from resampling the real EDM

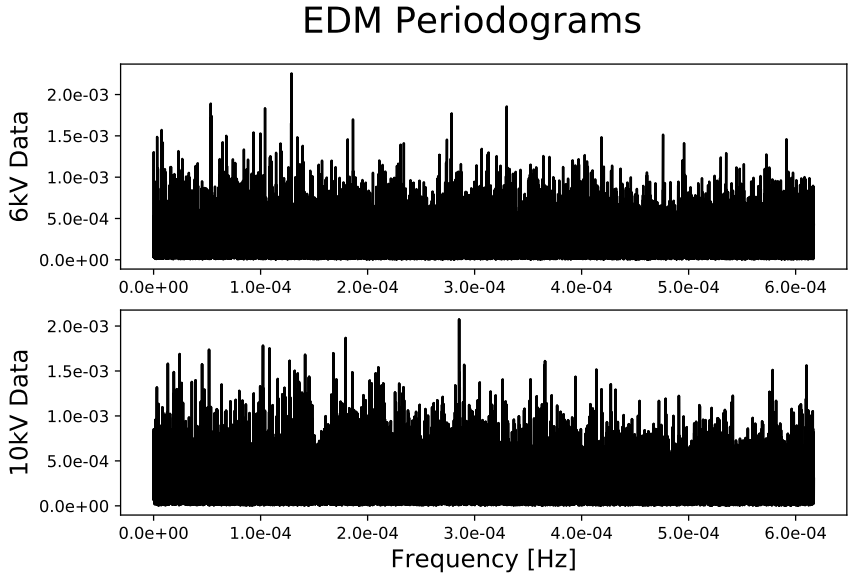

Figure 6.9: The first step of the second approach to EDM periodogram is to calculate the 6kV(top panel) and 10kV(bottom panel) periodograms separately.

data and see whether the peridogram of the resampled data can identify the fake signal as the maximum peak. The procedure is very similar to the way we obtain the maximum distribution using bootstrap method. The fake signal is injected in three resampled data sets after data points are randomly picked from three split groups of EDM data separately but with the same order. Then, we can calculate the periodograms of three resampled data and the averaged periodogram of the three.

The difference is we are interested in how well the periodgram of the resampled data with injecting fake signal can successfully detect the fake signal as the largest peak. Therefore, we collect the frequency of the maximum peak instead of maximum peak's magnitude in the periodgram. Repeating it many times gives us enough samples to conclude the probability of obtaining it as the largest peak in the periodgram with the given size and the given frequency of the fake signal. Fig.6.12 illustrates the steps to calculate the sensitivity of our measurement. In my analysis, I repeat 1,000 times for each injected signal and any maximum

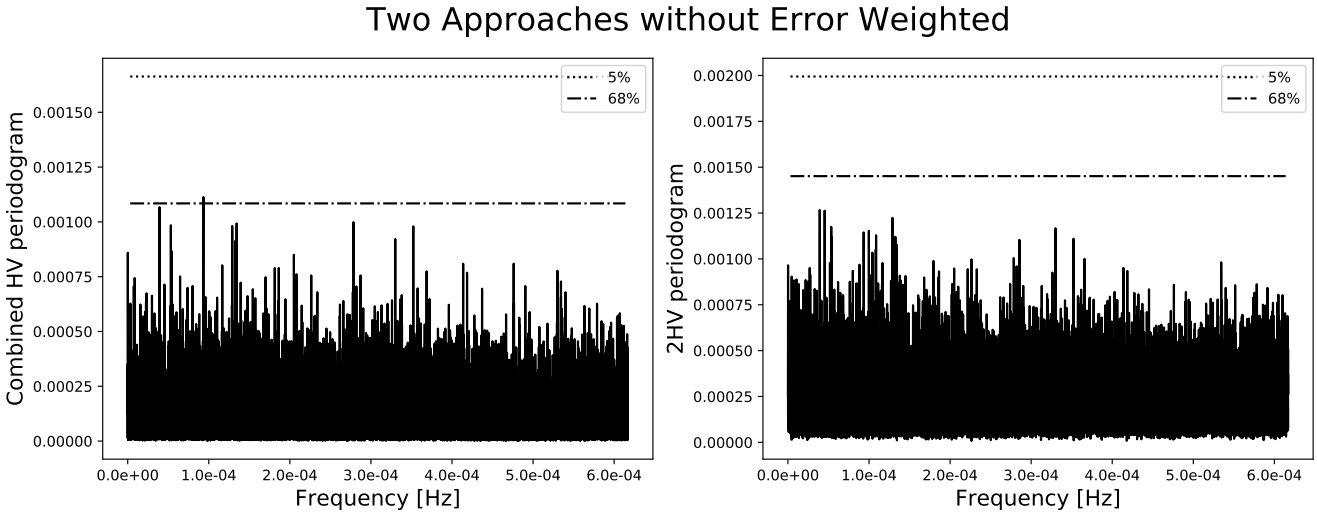

Figure 6.10: EDM periodograms without error weighted. The left panel is the Combined HV peridogoram with the maximum peak at 9.34×10^{-5} Hz with the FAP of 65%. The right panel is the 2HV peridogoram with the maximum peak at 3.92×10^{-5} Hz with the FAP of 94%. The horizontal lines are the FAP of the maximum peak at 5% and 0.3%.

peak locating within two frequency-grid size, $2 \times 4.99 \times 10^{-9}$ Hz, away from the correct frequency counts as successfully detected. Therefore, the sensitivity of the measurement with 95% confidence is defined by the size of the injected signal which can be detected as the maximum peak within $2 \times 4.99 \times 10^{-9}$ Hz accuracy with 95% probability in the periodograms of EDM bootstrap samples.

As a result, the four periodograms give similar results on the sensitivity of the measurement. For the case of the Combined HV Periodogram with error weighted shown in the left panel in Fig.6.13, the successful detection probability increases with increased amplitude of the signal but it does not seem to depend on the frequency of the signal. The lines in Fig.6.13 from top to bottom present the average probabilities of 95%, 89%, 77%, and 59% with the injected fake signal's amplitude being 2.3×10^{-29}, 2.14×10^{-29}, 1.98×10^{-29}, 1.81×10^{-29} $e \cdot cm$ at seven different frequencies. 2.3×10^{-29} $e \cdot cm$ is the sensitivity of our measurement with the first approach with error weighted to the EDM periodogram.

To estimate the size of the potential periodic signal in the EDM periodogram, I inject

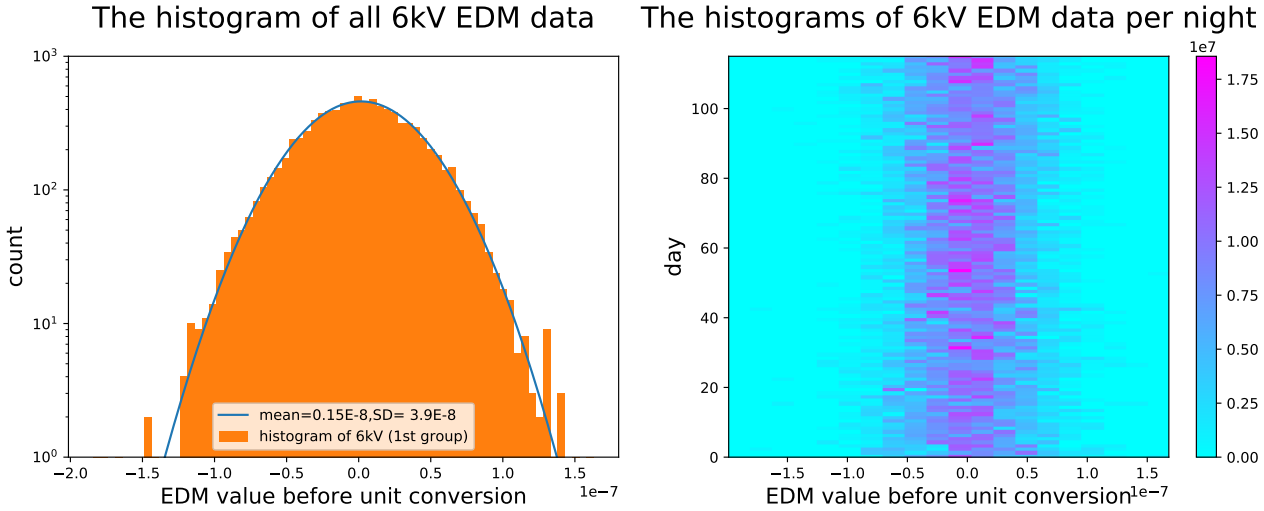

Figure 6.11: Comparison between the histogram of all 6kV data and the histograms of each night's 6kV data both from the first split group. The histogram of all 6kV data forms an almost perfect Gaussian function. But, each night's histogram shows the size of scatter varies by a small amount.

a fake signal with a given frequency into the resampled data and repeat it many times to take the average of magnitudes at that frequency in the peridograms. Fig.6.14 illustrates the procedure of estimating the size of signal with the bootstrap method. In the right panel of Fig.6.13, it shows the size of the peak in the periodogram increases with the size of the injected signal. It does not seem to be frequency dependent. Also, a signal with the magnitude of 1.27×10^{-3} can be generated in the error weighted Combined HV periodogram by a periodic signal with an amplitude of 1.81×10^{-29} $e \cdot cm$.

In conclusion, the four periodograms give a consistent result. None of them shows a significant detection on a periodic signal. The sensitivity of the four periodograms and the estimated signal size for the maximum peak are shown in Table 6.1. I take the result of the Combined HV Periodogram and conclude the sensitivity of the measurement is 2.3×10^{-29} $e \cdot cm$ with 95% confidence. The maximum peak in the periodogram is estimated be generated by a periodic signal with the magnitude of 1.81×10^{-29} $e \cdot cm$.

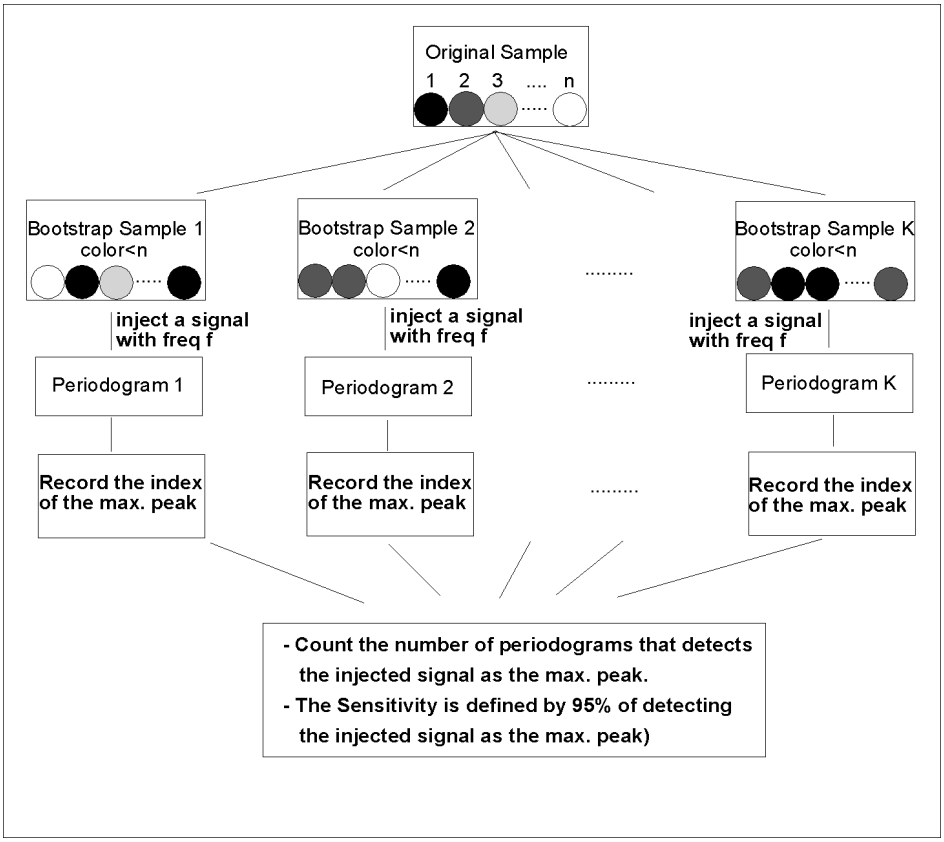

Figure 6.12: An illustration about calculating sensitivity of the measurement.

Oscillating ^{199}Hg EDM	FAP of max. peak	95% correct detection as max. peak $[\ e \cdot cm\ ]$	Estimated amplitude of max. peak $[\ e \cdot cm\ ]$
Combined HV with error	31%	2.3×10^{-29}	1.81×10^{-29}
2HV with error	82%	2.52×10^{-29}	1.81×10^{-29}
Combined HV without error	65%	3.4×10^{-29}	1.5×10^{-29}
2HV without error	94%	3.29×10^{-29}	1.3×10^{-29}

Table 6.1: A summary result of the four periodograms.

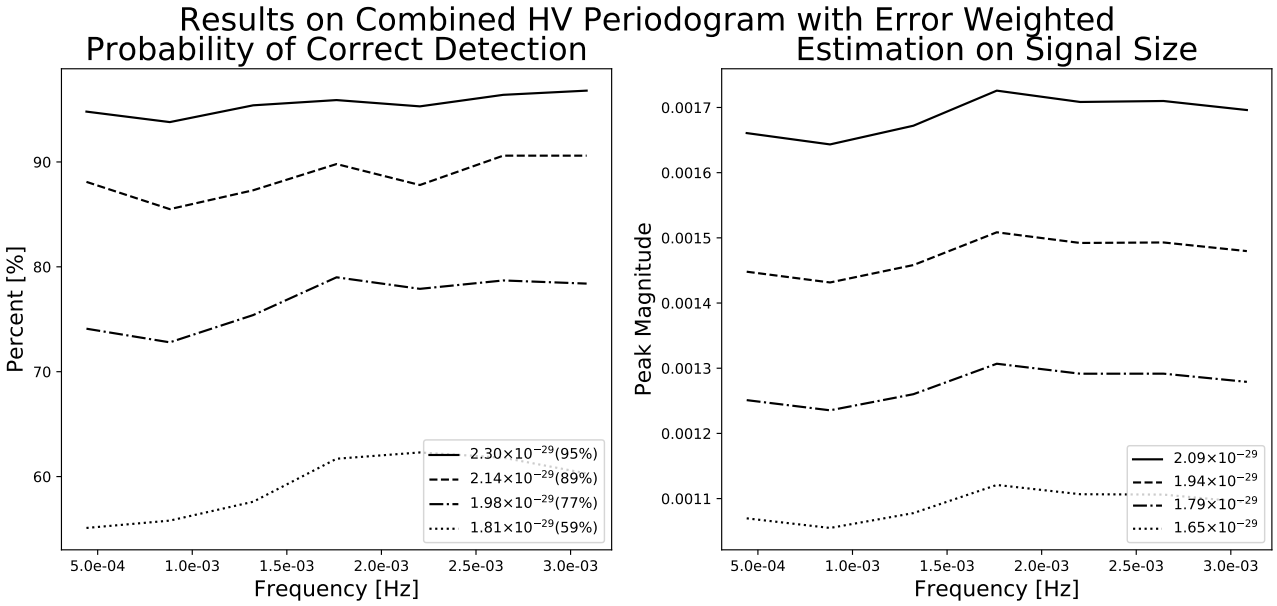

Figure 6.13: Both the sensitivity of the periodogram and the size of peak in the periodogram are not frequency dependent. The left panel shows the sensitivity of the error weighted Combined HV Periodogram in the frequency range 0 to 6.17×10^{-4} Hz is 2.3×10^{-29} $c \cdot cm$ with 95% confidence. The right panel shows the maximum peak in the periodogram can be generated by a periodic signal with the magnitude of 1.81×10^{-29} $e \cdot cm$.

6.2.1 Discussion on the two limits: static and oscillating

The EDM data puts a limit on both static and oscillating EDMs. For the static EDM, the statistical uncertainty is 2.75×10^{-30} $e \cdot cm$. The averaged magnitude of 2.88×10^{-29} $e \cdot cm$ is the limit on the oscillating EDM with 95% confidence.

These two numbers are trying to answer for two very different questions. To simplify the situation and understand where the factor of 10 comes from between these two limits, 1024 Gaussian-distributed points with zero mean, .5 standard deviation and evenly spaced in time without considering measurement uncertainties are used as an simulation. In this analysis, the data being evenly-spaced allows me use the L-S periodogram with psd normalization which is consistent with the Fourier power spectrum. Because the power is exponentially distributed and the power of a given frequency is proportional to its squared amplitude

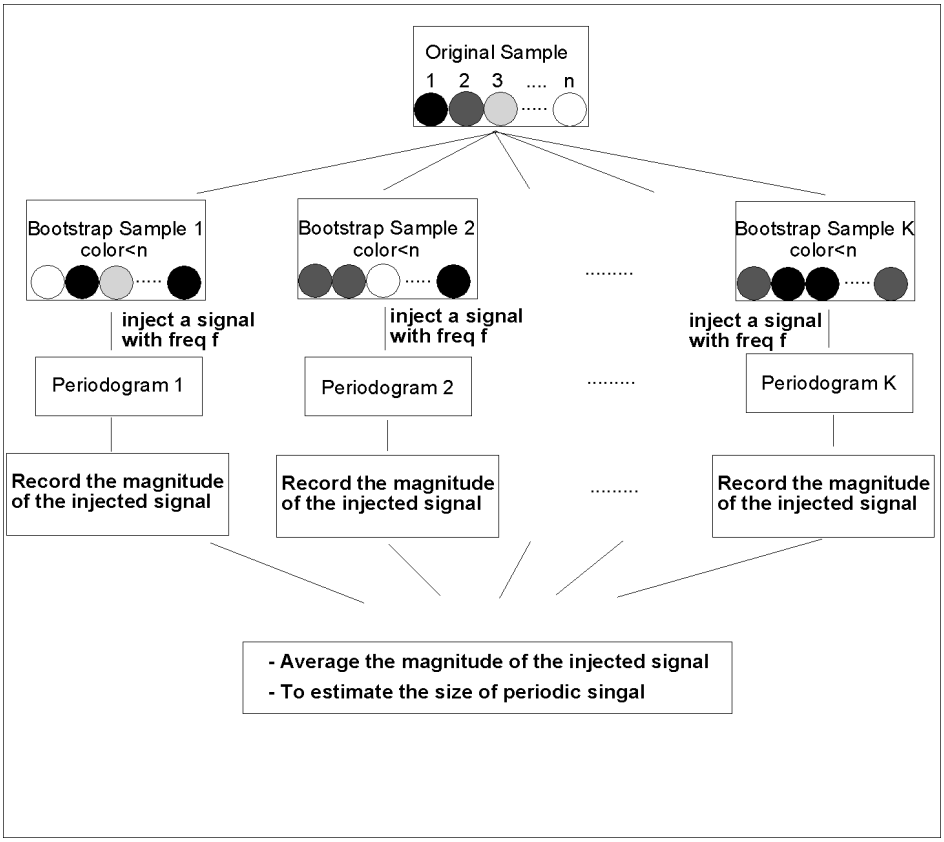

Figure 6.14: An illustration of procedure for estimating the size of the potential periodic signal.

of the signal, we can determine the oscillating signal corresponding to 95% of the power distribution in the periodogram is .054. It is a factor of 3.4 larger than the static limit, $\frac{\sigma}{\sqrt{number of points}} = \frac{0.5}{\sqrt{1000}} = 0.016$. By resampling this Gaussian distributed data and injecting a signal on top of it, the injected signal of .09 has a 95% probability of producing a peak greater than 95% of the power distribution. Furthermore, the amplitude of .12 has a 95% probability of obtaining its peak as the maximum peak in the periodogram of the resampled data. It is a factor of 7 larger than the static limit.

The sensitivity of EDM measurement is proportional to high voltage(HV) value. With two HV setups, 6k Volts and 10k Volts, the EDM measurment is expected to be two Gaussian distributed data with the corresponding standard deviation to be $\frac{10}{6}\sigma$ and σ. Taking the HV

into account, the simulated data has two sets of 512 Gaussian-distributed data with standard deviations of 0.5 and $0.5 \times \frac{10}{6}$. As the result on resampled data with an injected signal, a signal of .16 has 95% probability of obtaining the injected signal as the maximum peak in the periodogram. It is a factor of 10 comparing to the static limit.

To compare the limits between static one and oscillating one, the simulated data has to be evenly spaced in time. That is because the statistical properties of periodogram with psd normalization no longer holds when the time is not evenly spaced. The periodogram with standard normalization takes the standard deviation of the data into account so the injected periodic signal changes the overall shape of the power distribution. Also, FAP in the L-S periodogram is used to look for the probability of obtaining a peak with such magnitude assuming there is no periodic signal. L-S periodogram cannot tell the size of the signal causing a specific peak in the periodogram.

BIBLIOGRAPHY

[1] PAR Ade, N Aghanim, M Arnaud, M Ashdown, J Aumont, C Baccigalupi, AJ Banday, RB Barreiro, N Bartolo, E Battaner, et al. Planck 2015 results-xiv. dark energy and modified gravity. *Astronomy & Astrophysics*, 594:A14, 2016.

[2] Irshad Ahmad and PA Butler. Octupole shapes in nuclei. *Annual Review of Nuclear and Particle Science*, 43(1):71–116, 1993.

[3] DS Akerib, S Alsum, HM Araújo, X Bai, AJ Bailey, J Balajthy, P Beltrame, EP Bernard, A Bernstein, TP Biesiadzinski, et al. Results from a search for dark matter in the complete lux exposure. *Physical review letters*, 118(2):021303, 2017.

[4] E Aprile, J Aalbers, F Agostini, M Alfonsi, FD Amaro, M Anthony, F Arneodo, P Barrow, L Baudis, Boris Bauermeister, et al. First dark matter search results from the xenon1t experiment. *Physical review letters*, 119(18):181301, 2017.

[5] Howard Baer, Ki-Young Choi, Jihn E Kim, and Leszek Roszkowski. Dark matter production in the early universe: beyond the thermal wimp paradigm. *Physics Reports*, 555:1–60, 2015.

[6] CA Baker, Y Chibane, M Chouder, P Geltenbort, K Green, PG Harris, BR Heckel, P Iaydjiev, SN Ivanov, I Kilvington, et al. Apparatus for measurement of the electric dipole moment of the neutron using a cohabiting atomic-mercury magnetometer. *Nuclear Instruments and Methods in Physics Research Section A: Accelerators, Spectrometers, Detectors and Associated Equipment*, 736:184–203, 2014.

[7] Roman V Baluev. Assessing the statistical significance of periodogram peaks. *Monthly Notices of the Royal Astronomical Society*, 385(3):1279–1285, 2008.

[8] Michael Bishof, Richard H Parker, Kevin G Bailey, John P Greene, Roy J Holt, Mukut R Kalita, Wolfgang Korsch, Nathan D Lemke, Zheng-Tian Lu, Peter Mueller, et al. Improved limit on the ra 225 electric dipole moment. *Physical Review C*, 94(2):025501, 2016.

[9] Whitney Clavin and JD Harrington. Planck mission brings universe into sharp focus. *Jet Propulsion Laboratory: California Institute of Technology, http:// www. jpl. nasa. gov/ news/ news. php*, 2013.

[10] Jan Conrad, Johann Cohen-Tanugi, and Louis E Strigari. Wimp searches with gamma rays in the fermi era: challenges, methods and results. *Journal of Experimental and Theoretical Physics*, 121(6):1104–1135, 2015.

[11] A Cumming. Mnras, 354, 1165. *arXiv preprint astro-ph/0408470*, 2004.

[12] Andrew Cumming, Geoffrey W Marcy, and R Paul Butler. The lick planet search: detectability and mass thresholds. *The Astrophysical Journal*, 526(2):890, 1999.

[13] Jonas Debosscher, LM Sarro, Conny Aerts, J Cuypers, Bart Vandenbussche, R Garrido, and E Solano. Automated supervised classification of variable stars-i. methodology. *Astronomy & Astrophysics*, 475(3):1159–1183, 2007.

[14] N Du, N Force, R Khatiwada, E Lentz, R Ottens, LJ Rosenberg, Gray Rybka, G Carosi, N Woollett, D Bowring, et al. Search for invisible axion dark matter with the axion dark matter experiment. *Physical review letters*, 120(15):151301, 2018.

[15] Bradley Efron. Computers and the theory of statistics: thinking the unthinkable. *SIAM review*, 21(4):460–480, 1979.

[16] G Feinberg. Parity-violating electromagnetic interactions of nuclei. *Transactions of the New York Academy of Sciences*, 38(1 Series II):26–43, 1977.

[17] S Ferraz-Mello. Estimation of periods from unequally spaced observations. *The Astronomical Journal*, 86:619, 1981.

[18] FAM Frescura, CA Engelbrecht, and BS Frank. Significance of periodogram peaks and a pulsation mode analysis of the beta cephei star v403 car. *Monthly Notices of the Royal Astronomical Society*, 388(4):1693–1707, 2008.

[19] Ronald L Gilliland and Sallie L Baliunas. Objective characterization of stellar activity cycles. i-methods and solar cycle analyses. *The Astrophysical Journal*, 314:766–781, 1987.

[20] JSM Ginges and Victor V Flambaum. Violations of fundamental symmetries in atoms and tests of unification theories of elementary particles. *Physics Reports*, 397(2):63–154, 2004.

[21] Peter W Graham and Surjeet Rajendran. Axion dark matter detection with cold molecules. *Physical Review D*, 84(5):055013, 2011.

[22] Peter W Graham and Surjeet Rajendran. New observables for direct detection of axion dark matter. *Physical Review D*, 88(3):035023, 2013.

[23] B Graner, Y Chen, EG Lindahl, and BR Heckel. Reduced limit on the permanent electric dipole moment of hg 199. *Physical review letters*, 116(16):161601, 2016.

[24] Brent Graner. *Reduced Limit on the Permanent Electric Dipole Moment of 199Hg*. PhD thesis, University of Washington, 2017.

[25] James H Horne and Sallie L Baliunas. A prescription for period analysis of unevenly sampled time series. *The Astrophysical Journal*, 302:757–763, 1986.

[26] Alan W Irwin, Bruce Campbell, Christopher L Morbey, GAH Walker, and S Yang. Long-period radial-velocity variations of arcturus. *Publications of the Astronomical Society of the Pacific*, 101(636):147, 1989.

[27] Željko Ivezić, Andrew J Connolly, Jacob T VanderPlas, and Alexander Gray. *Statistics, Data Mining, and Machine Learning in Astronomy: A Practical Python Guide for the Analysis of Survey Data*. Princeton University Press, 2014.

[28] Nicholas R Lomb. Least-squares frequency analysis of unequally spaced data. *Astrophysics and space science*, 39(2):447–462, 1976.

[29] Athanasios Papoulis. *Probability, Random Variables, and Stochastic Processes: Solutions to the Problems in Probability, Random Variables and Stochastic Processes*. McGraw-Hill, 1965.

[30] Roberto D Peccei and Helen R Quinn. Constraints imposed by cp conservation in the presence of pseudoparticles. *Physical Review D*, 16(6):1791, 1977.

[31] Roberto D Peccei and Helen R Quinn. Cp conservation in the presence of pseudoparticles. *Physical Review Letters*, 38(25):1440, 1977.

[32] JM Pendlebury, S Afach, NJ Ayres, CA Baker, G Ban, Georg Bison, Kazimierz Bodek, M Burghoff, P Geltenbort, K Green, et al. Revised experimental upper limit on the electric dipole moment of the neutron. *Physical Review D*, 92(9):092003, 2015.

[33] Joseph W Richards, Dan L Starr, Adam A Miller, Joshua S Bloom, Nathaniel R Butler, Henrik Brink, and Arien Crellin-Quick. Construction of a calibrated probabilistic classification catalog: Application to 50k variable sources in the all-sky automated survey. *The Astrophysical Journal Supplement Series*, 203(2):32, 2012.

[34] Leszek Roszkowski, Enrico Maria Sessolo, and Sebastian Trojanowski. Wimp dark matter candidates and searchescurrent status and future prospects. *Reports on Progress in Physics*, 81(6):066201, 2018.

[35] Vera C Rubin and W Kent Ford Jr. Rotation of the andromeda nebula from a spectroscopic survey of emission regions. *The Astrophysical Journal*, 159:379, 1970.

[36] Andrei D Sakharov. Violation of cp invariance, c asymmetry, and baryon asymmetry of the universe. *Soviet Physics Uspekhi*, 34(5):392, 1991.

[37] Jeffrey D Scargle. Studies in astronomical time series analysis. ii-statistical aspects of spectral analysis of unevenly spaced data. *The Astrophysical Journal*, 263:835–853, 1982.

[38] Jeffrey D Scargle. Studies in astronomical time series analysis. iii-fourier transforms, autocorrelation functions, and cross-correlation functions of unevenly spaced data. *The Astrophysical Journal*, 343:874–887, 1989.

[39] LI Schiff. Measurability of nuclear electric dipole moments. *Physical Review*, 132(5):2194, 1963.

[40] A Schwarzenberg-Czerny. Fast and statistically optimal period search in uneven sampled observations. *The Astrophysical Journal Letters*, 460(2):L107, 1996.

[41] V Spevak, N Auerbach, and VV Flambaum. Enhanced t-odd, p-odd electromagnetic moments in reflection asymmetric nuclei. *Physical Review C*, 56(3):1357, 1997.

[42] Jacob T VanderPlas. Understanding the lomb-scargle periodogram. *arXiv preprint arXiv:1703.09824*, 2017.

[43] Jacob T VanderPlas and Željko Ivezic. Periodograms for multiband astronomical time series. *The Astrophysical Journal*, 812(1):18, 2015.

[44] David E Wells, Petr Vaníček, and Spiros Demitris Pagiatakis. *Least squares spectral analysis revisited*. Department of Surveying Engineering, University of New Brunswick, 1985.

[45] M Zechmeister and M Kürster. The generalised lomb-scargle periodogram-a new formalism for the floating-mean and keplerian periodograms. *Astronomy & Astrophysics*, 496(2):577–584, 2009.